Intensification Rates of Tropical Cyclone-Like Vortices in a Model with

Down-Tilt Diabatic Forcing and Oceanic Surface Drag

David A. Schecter^{1*}

- ¹NorthWest Research Associates, Boulder, Colorado, USA
- Submitted to Journal of the Atmospheric Sciences August 30, 2022; accepted March 10, 2023
- DOI for the published journal article with final edits: 10.1175/JAS-D-22-0188.1.

^{*}Corresponding author address: NorthWest Research Associates, 3380 Mitchell Lane, Boulder, CO, USA, 80301. E-mail: schecter@nwra.com

Tropical cyclones are commonly observed to have appreciable vertical misalign-ABSTRACT: ments prior to becoming full-strength hurricanes. The vertical misalignment (tilt) of a tropical cyclone is generally coupled to a pronounced asymmetry of inner-core convection, with the strongest 10 convection tending to concentrate down-tilt of the surface vortex center. Neither the mechanisms by which tilted tropical cyclones intensify nor the time scales over which such mechanisms operate 12 are fully understood. The present study offers some insight into the asymmetric intensification 13 process by examining the responses of tilted tropical cyclone-like vortices to down-tilt diabatic forcing (heating) in a 3D nonhydrostatic numerical model. The magnitude of the heating is adjusted so as to vary the strength of the down-tilt convection that it generates. A fairly consistent picture of intensification is found in various simulation groups that differ in their initial vortex 17 configurations, environmental shear flows, and specific positionings of down-tilt heating. The 18 intensification mechanism generally depends on whether the low-level convergence σ_b produced 19 in the vicinity of the down-tilt heat source exceeds a critical value dependent on the local veloc-20 ity of the low-level nondivergent background flow in a reference frame that drifts with the heat source. Supercritical σ_b causes fast spinup initiated by down-tilt core replacement. Subcritical 22 σ_b causes a slower intensification process. As measured herein, the supercritical intensification rate is approximately proportional to σ_b . The subcritical intensification rate has a more subtle scaling, and expectedly becomes negative when σ_b drops below a threshold for frictional spindown 25 to dominate. The relevance of the foregoing results to real-world tropical cyclones is discussed.

1. Introduction

9

Tropical cyclone intensification theory has a long and venerable history [Montgomery and 10 Smith 2014; Emanuel 2018], but has largely focused on simplified models in which the vortex is vertically aligned and the internal moist convection is either purely or statistically axisymmetric. 12 While such a focus has facilitated progress toward understanding the thermo-fluid dynamics 13 of intensification, it manifestly neglects an entire dimension of the problem. The author of the present article contends that a comprehensive conceptual understanding of tropical cyclone intensification must take into account the common reality of vortex misalignment (tilt) and the associated asymmetric distribution of moist convection. Such violation of the traditional 17 theoretical assumption of axisymmetric structure can be especially pronounced during the pre-hurricane phases of intensification [e.g., Fischer et al. 2022], when the vortex seems most 19 prone to having considerable tilt in association with exposure to a moderate degree of transient or 20 sustained environmental vertical wind shear [e.g., Jones 1995; Reasor et al. 2004].

The effects of tilt on tropical cyclone intensification have been examined to some extent in the 22 past, but have not been fully elucidated. Numerous studies have suggested that an appreciable tilt 23 will generally slow or even neutralize low-level spinup [e.g., DeMaria 1996; Riemer et al. 2010; Rappin and Nolan 2012; Tao and Zhang 2014; Finnochio et al. 2016; Rios-Berrios et al. 2018; 25 Schecter and Menelaou 2020 (SM20); Fischer et al. 2021; Schecter 2022 (S22)]. On the other hand, tilted systems with sufficiently strong down-tilt convection have been known to occasionally exhibit core reformation followed by rapid intensification [e.g., Molinari et al. 2004; Molinari and Vollaro 2010; Nguyen and Molinari 2015; Chen et al. 2018; Alvey et al. 2022]. Regarding the common scenario of slow spinup, there does not yet exist a comprehensive quantitative theory for 30 the dependence of the intensification rate on relevant parameters of the tilted system. Moreover, there may be a number of distinct slow modes of asymmetric intensification that have not yet been 32 discovered or explicitly recognized. Although a quantitative condition for fast spinup initiated by 33 core reformation has been proposed, there are still questions as to whether the underlying theory is adequate (see below). The essential purpose of the present study is to advance our current 35 quantitative understanding of the distinct intensification mechanisms available to tilted tropical cyclones, their conditions of applicability, and their operational time scales.

The approach adopted herein is to consider a simplified fluid dynamical system that facilitates 38 experimental control over the convection that drives intensification. In particular, this study 39 considers a dry three-dimensional vortex that is misaligned and subjected to parameterized diabatic 4۱ forcing that generates deep convection concentrated down-tilt of the surface vortex center for basic consistency with observations [cf. Reasor et al. 2013; Stevenson et al. 2014; Nguyen et al. 2017]. 42 The specifics of the heating distribution and the coupling of its center to the continuously changing tilt vector of the vortex are varied so as to cover a range of possibilities that are potentially relevant to tropical cyclones in nature and in cloud resolving simulations under a variety of environmental conditions. A standard oceanic surface drag parameterization is generally implemented, but its role is limited to that of an agent of kinetic energy dissipation; the regulatory influence of Ekman-like pumping on the heating distribution is not directly incorporated into the model. Indeed, the model under present consideration cannot answer questions regarding what regulates the local spatio-49 temporal properties of the heating distribution, nor what regulates the relationship between the 50 heating center and the tilt vector. Such issues can only be investigated through observational and full-physics modeling studies, and have been extensively (albeit incompletely) addressed elsewhere [see many of the previous references, along with (for example) Zawislak et al. 2016; Onderlinde 53 and Nolan 2016; Gu et al. 2019; Alvey et al. 2020; Rogers et al. 2020; Alland et al. 2022ab]. The questions to be answered herein are limited to those concerning how intensification varies with the 55 parameters characterizing the nature of the asymmetric internal heating. 56

Schecter 2020 [S20] provided some preliminary insights into what to expect from the present study. To elaborate, S20 considered a shallow-water vortex representing the low-level circulation of a tropical cyclone, forced by an off-center mass sink representing down-tilt convection. The mechanism and time scale of vortex intensification expectedly varied with the velocity convergence generated by (and colocated with) the mass sink. The prevailing intensification mechanism was largely determined by whether the magnitude of convergence exceeds a critical value dependent on the spatial extent of the mass sink, the drift velocity of the mass sink, and the contribution to the local flow velocity from the larger scale cyclonic circulation. Supercritical convergence horizontally trapped fluid undergoing vorticity amplification inside the mass sink, whereas subcritical convergence allowed the fluid to escape and recirculate around the broader cyclone. When having supercritical strength, a convergence zone displaced from the central region of the cyclone gener-

ally induced on-site reformation of the vortex core followed by fast intensification. The process notably resembled the initiation of fast spinup through core reformation that—as mentioned earlier—is occasionally seen in real and realistically simulated tropical cyclones. Vortices possessing subcritical convergence zones were found to follow one of two slower pathways of development. One of the slower modes of intensification entailed a gradual merger of the vortex center with the convergence zone, coinciding with a gradual reduction of the radius of maximum azimuthal velocity r_m . The other involved no such merger, nor any appreciable change of r_m .

The extent to which the results of S20 should carry over to the model under present consideration is not entirely obvious. To begin with, the presence of horizontal vorticity and the associated vertical differential advection in a three-dimensional tropical cyclone-like vortex could substantially alter the production of vertical vorticity in the convection zone and its subsequent evolution. Moreover, the inclusion of surface drag (absent in S20) should provide an effective counterbalance to slow intensification mechanisms, and possibly cause spindown. One important issue to be addressed is whether the critical low-level convergence required for core reformation remains consistent with the S20 shallow-water theory. Another issue to be addressed is the extent to which three-dimensionality and surface friction alter the nature of subcritical intensification and its dependence on the properties of the low-level convergence zone associated with down-tilt convection.

Needless to say, S20 and the present study are not the first to consider the intensification of tropical cyclone-like vortices resulting from experimentally controlled diabatic forcing. This approach has been used extensively in the context of axisymmetric models, and has shown *inter alia* that heat sources tend to more efficiently intensify vortices when situated in regions of relatively high inertial stability near or inward of the radius of maximum wind speed [Vigh and Schubert 2009; Pendergrass and Willoughby 2009]. There have also been fully-3D studies of vortex intensification resulting from various forms of asymmetric diabatic forcing. Some of the aforementioned studies have focused on quasi-linear dynamics [e.g., Nolan et al. 2007], while others have employed models that include stronger nonlinear effects [Dörffel et al. 2021 (D21); Päschke et al. 2012]. The quasi-linear models have been useful for assessing the extent to which waves induced by asymmetric diabatic forcing influence the azimuthal-mean flow of the vortex and thereby change its maximum tangential wind speed. However, quasi-linear models cannot be used to investigate some of the highly nonlinear processes of present interest, such as those associated with core

reformation. D21 can be seen to have some features in common with the present study, in using a nonlinear model and in prescribing the asymmetric diabatic forcing in relation to the tilt of the tropical cyclone-like vortex. On the other hand, owing to its distinct theoretical objectives, the case studies of D21 used broad dipolar heating instead of predominantly positive heating concentrated down-tilt of the surface center, provisionally neglected surface friction, and did not explicitly address core reformation.

There exists another simplified experimental approach for investigating the pathways of tropical 104 cyclone intensification driven by off-center localized convection— not necessarily associated with 105 tilt —that merits brief discussion. Instead of directly forcing the system with a heat source, 106 clustered vorticity perturbations representing the product of localized convection can be added 107 to the broader cyclonic circulation at time intervals deemed consistent with natural convective 108 pulsing. Past studies adopting this approach have paid considerable attention to how angular 109 momentum is redistributed by vortex Rossby waves (or subvortices) following the episodes of 110 convection that create the vorticity anomalies [Montgomery and Enagonio 1998; Möller and Montgomery 1999,2000; Enagonio and Montgomery 2001]. These studies have also examined the 112 intensity required for a vorticity anomaly to supplant the core of a parent cyclone [Enagonio and 113 Montgomery 2001]. The present study [and S20] can be seen to complement those just described by taking a step toward elucidating the efficiency of vorticity build-up in the convergence zone 115 associated with convection, and how that efficiency affects the pathway of intensification. 116

The remainder of this paper is organized as follows. Section 2 describes the model used for the present study, and provides an overview of the numerical experiments. Section 3 describes the results of the numerical experiments. Differences between subcritical and supercritical intensification are illustrated. Distinct scalings for subcritical and supercritical intensification rates are presented. Section 4 relates the results of section 3 to real-world and realistically simulated tropical cyclone dynamics. Section 5 summarizes all main findings of the study.

117

119

120

122

123

2. Basic Methodology

2a. The Model Used to Simulate Tilted "Tropical Cyclones"

124

125

127

142

145

146

149

The objectives of this study are achieved primarily through numerical simulations of tropical 128 cyclone-like vortex intensification conducted with a simplified version of release 19.5 of Cloud 129 Model 1 [CM1; Bryan and Fritsch 2002]. CM1 is a widely used nonhydrostatic atmospheric model with high precision numerics and conventional parameterizations of subgrid turbulent transport, 131 cloud microphysics and radiative transfer. Herein, the latter two features are deactivated. The re-132 sulting dry model is forced with an adjustable source term in the potential temperature (θ) tendency 133 equation that substitutes primarily for down-tilt moist-convective heating (see below). Subgrid 134 turbulent transport above the surface layer is represented by an anisotropic Smagorinsky-type pa-135 rameterization specified in section 2a of SM20. Surface momentum fluxes are represented by a bulk-136 aerodynamic formula appropriate for oceanic systems, in which the drag coefficient C_d increases from a minimum value of 0.001 to a maximum value of 0.0024 as the surface wind speed increases 138 from 5 to 25 m s⁻¹. Surface enthalpy fluxes are invariably turned off. Rayleigh perturbationdamping is applied for z > 25 km, in which z denotes height above sea-level. All simulations are set up on a doubly-periodic f-plane with a Coriolis parameter given by $f = 5 \times 10^{-5} \text{ s}^{-1}$. 141

The equations of motion are discretized on a stretched rectangular grid that spans 2660 km in both horizontal dimensions, and extends upward to z = 29.2 km. The 800×800 km² central region of the horizontal mesh that contains the tilted vortex core has uniform increments of 2.5 km; at the four corners of the mesh, the increments are 27.5 km. The vertical grid has 40 levels spaced apart by distances that increase from 0.1 to 0.7 to 1.4 km as z increases from 0 to 8 to 29 km.

The source term added to the equation for the material derivative of potential temperature $(D\theta/Dt)$ is of the form

$$\dot{\theta}_f \equiv a \exp\{-(\tilde{r}/\delta r_f)^2 - [(z - z_f)/\delta z_f^{\pm}]^2\} T(t; \delta \tau_f), \tag{1}$$

in which a is the strength parameter, \tilde{r} is radius measured in the horizontal plane from the forcing center \mathbf{x}_f , δr_f is the radial lengthscale of the forcing, and z_f is the height of maximum forcing.

The symbol δz_f^{\pm} represents the upper vertical lengthscale (δz_f^{+}) of the forcing if $z > z_f$, or the

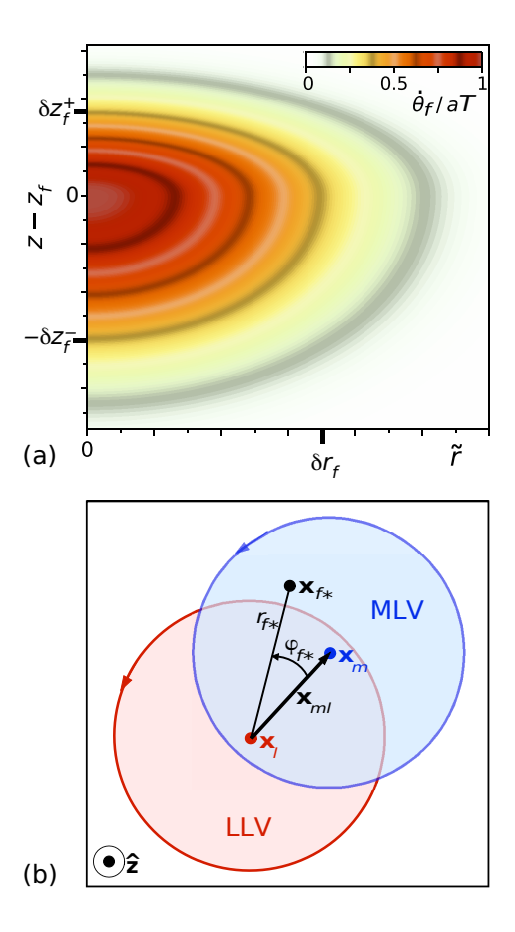


Fig. 1: (a) Normalized heating distribution $\dot{\theta}_f/aT$ with typical vertical asymmetry characterized by $\delta z_f^+ = 7\delta z_f^-/12$. (b) Diagram showing the polar coordinates r_{f*} and φ_{f*} of an arbitrarily placed target position for the heat source \mathbf{x}_{f*} . The polar coordinate system has its origin at the center \mathbf{x}_l of the red low-level vortex (LLV), and is oriented such that φ_{f*} is zero in the direction of the tilt vector \mathbf{x}_{ml} , which points from \mathbf{x}_l to the center \mathbf{x}_m of the blue midlevel vortex (MLV).

lower vertical lengthscale (δz_f^-) if $z < z_f$. The last factor is a ramp function of time t, defined by $T \equiv \max(t/\delta \tau_f, 0)$ for $t < \delta \tau_f$ and $T \equiv 1$ for $t \ge \delta \tau_f$. Figure 1a shows $\dot{\theta}_f/aT$ for a case with typical vertical asymmetry about z_f . In general, z_f lies in the middle-to-upper troposphere, and the downward decay length (δz_f^-) is of comparable magnitude [see section 2c].

The forcing center is governed by the following prognostic equation:

158

$$\frac{d\mathbf{x}_f}{dt} = -\frac{\mathbf{x}_f - \mathbf{x}_{f*}}{\tau_f},\tag{2}$$

in which τ_f is a relaxation time and $\mathbf{x}_{f*}(t)$ is a moving target for \mathbf{x}_f that usually lies in the vicinity of the midlevel vortex center \mathbf{x}_m . Without exception, \mathbf{x}_f is initialized to \mathbf{x}_{f*} at t = 0. In general,

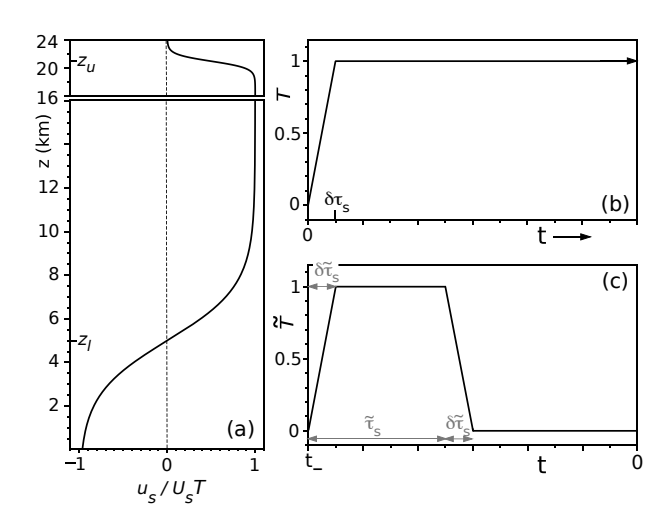


Fig. 2: (a) The normalized velocity u_s/U_sT (solid curve) and (b) the time factor T of the shear flow [Eq. (4)] that is applied after t = 0 to a subset of simulations. (c) The time factor \tilde{T} that is substituted for T in Eq. (4) for the preparatory shear flow that creates the initial tilt of each tropical-cyclone like vortex [see section 2b].

 \mathbf{x}_{f*} is specified by its radius r_{f*} and azimuth φ_{f*} in a polar coordinate system [Fig. 1b] whose origin is at the low-level vortex center \mathbf{x}_l , and whose orientation continuously changes to keep the zero azimuth along the direction of the evolving tilt vector $\mathbf{x}_{ml} \equiv \mathbf{x}_m - \mathbf{x}_l$. The trajectories of \mathbf{x}_m and \mathbf{x}_l are tracked while the simulation runs. The reader may consult appendix A for details on the computations of \mathbf{x}_l and \mathbf{x}_m .

A subset of simulations include additional forcing on the right-hand side of the horizontal velocity (**u**) tendency equation of the form

$$\mathbf{F}_{s} \equiv \frac{\partial u_{s}}{\partial t} \hat{\mathbf{e}}_{s} + f u_{s} \hat{\mathbf{z}} \times \hat{\mathbf{e}}_{s}. \tag{3}$$

The purpose of \mathbf{F}_s is to generate and sustain an ambient shear flow coaligned with the fixed unit vector $\hat{\mathbf{e}}_s$ in the horizontal plane. The shear flow is given by

168

171

$$u_s(z,t) = \frac{U_s}{2} \tanh\left(\frac{z - z_l}{\delta z_l}\right) \left[1 + \tanh\left(\frac{z_u - z}{\delta z_u}\right)\right] T(t; \delta \tau_s),\tag{4}$$

in which U_s is an adjustable maximum wind speed, $z_l = 5$ km is the center of the primary shear layer, $\delta z_l = 2.5$ km is the half-width of the primary shear layer, and $z_u = 21$ km is the upper altitude at which the shear flow decays toward zero with increasing height over a lengthscale δz_u

¹Thus, for example, the combination $r_{f*} = |\mathbf{x}_{ml}|$ and $\varphi_{f*} = 0$ would imply that $\mathbf{x}_{f*} = \mathbf{x}_m$.

of 1 km. The last factor T is the temporal ramp function defined previously, but with $\delta \tau_f$ replaced by $\delta \tau_s = 1$ h. Figures 2a and 2b respectively illustrate the dependencies of u_s on height and time. 176 Along with \mathbf{F}_s , Rayleigh damping of the form $\mathbf{F}_d \equiv -(\mathbf{u} - u_s \hat{\mathbf{e}}_s) \Upsilon_d(\check{r}; r_d, \delta r_d) / \delta \tau_d$ is added to the 177 right-hand side of the equation for $\partial \mathbf{u}/\partial t$ in the periphery of the simulation domain to prevent sheared-away structures from re-entering the system as a result of periodic boundary conditions. 179 The dependence of the damping on radius \check{r} from the domain center is given by $\Upsilon_d = 0$ for $\check{r} \leq r_d$, 180 and $\Upsilon_d = \{1 - \cos[\pi \min(\check{r} - r_d, \delta r_d)/\delta r_d]\}/2$ for $\check{r} \ge r_d$. In all simulations with applied shear flows, $r_d = 1230$ km, $\delta r_d = 100$ km, and $\delta \tau_d = 300$ s. Note that the present methodology used for 182 imposing the ambient shear flow excludes the coupled horizontal potential temperature gradient 183 that would be found in nature to maintain thermal wind balance [cf. Nolan 2011]. Note also that the invariant vertical structure of the ambient shear flow used for the present study clearly limits 185 sensitivity tests to those involving variations of the magnitude (U_s) and orientation $(\hat{\mathbf{e}}_s)$ of the 186 velocity field. Efforts to ascertain the sensitivities of vortex intensification to structural details of 187 the shear flow, akin to those previously conducted with cloud resolving models [e.g., Finocchio et al. 2016; Onderlinde et al. 2016; Gu et al. 2019; Fu et al. 2019], will be deferred to a future time. 189

2b. Simulation Preparation

190

192

199

Each simulation is conducted in two stages. The first stage occurring over the interval $t_{-} \le t < 0$ involves initialization and vertical misalignment of the vortex. The second stage occurring for $t \ge 0$ involves the evolution of the vortex under the influence of diabatic forcing. The present subsection of this article pertains to the first stage of the simulation.

At $t = t_{-}$, the system is initialized with an axisymmetric baroclinic vortex in a stably stratified atmosphere [Fig. 3]. The vertical vorticity of this "original vortex" has the following form:

$$\zeta(r,z) = \left\{ \zeta_o e^{-(r/r_o)^2} \cos \left[\frac{\pi(z - z_o)}{2\delta z_o^+} \right] - \zeta_c(z) \right\} H(r_b - r) H(z_o + \delta z_o^+ - z), \tag{5}$$

in which r is radius from the vortex center, $r_o = 91$ km, $z_o = 3$ km, $\delta z_o^{\pm} \equiv \delta z_o^{+} (\delta z_o^{-})$ for $z > z_o$ ($z < z_o$), $\delta z_o^{+} = 11$ km, and δz_o^{-} has an effectively infinite value of 332.2 km. The Heaviside step function is defined by $H(x) \equiv 1$ (0) for x > 0 (x < 0). The small vorticity correction ($-\zeta_c$) brings the azimuthal velocity velocity $v(r,z) = \int_0^r dr' r' \zeta(r',z)/r$ to zero at $r = r_b = 750$ km. The maximum azimuthal velocity

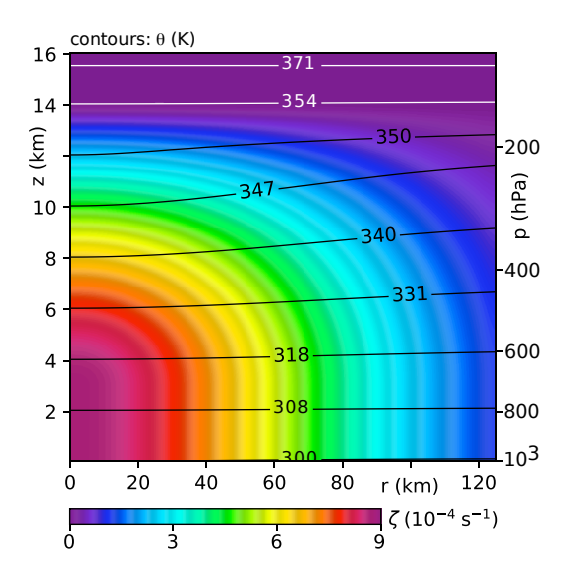


Fig. 3: The relative vertical vorticity (color) and potential temperature (contours) of the original balanced vortex for simulations with $\zeta_o = 8.837 \times 10^{-4} \text{ s}^{-1}$. The right edge of the plot shows the atmospheric pressure p at r = 125 km for selected values of z.

 v_{mo} occurs at the radius $r_{mo} = 100$ km and the altitude z_o . The v-field varies minimally below z_o , but gradually decays above z_o until reaching zero at z = 14 km. Most simulations are prepared with $\zeta_o = 8.837 \times 10^{-4} \text{ s}^{-1}$, in which case $v_{mo} = 25 \text{ m s}^{-1}$. The vertical distributions of pressure and θ outside the vortex $(r > r_b)$ match those of the Dunion [2011] moist tropical sounding. Within the vortex, the aforementioned fields are adjusted to satisfy gradient and hydrostatic balance conditions consistent with v.

The vortex is subsequently tilted by a transient shear flow generated by a forcing term $\tilde{\mathbf{F}}_s$ on the right-hand side of the $\partial \mathbf{u}/\partial t$ equation that is similar to \mathbf{F}_s [Eqs. (3)-(4)], but with the time-factor T replaced by

$$\tilde{T}(\tilde{t}; \tilde{\tau}_{s}, \delta \tilde{\tau}_{s}) \equiv \begin{cases}
\tilde{t}/\delta \tilde{\tau}_{s} & 0 \leq \tilde{t} < \delta \tilde{\tau}_{s}, \\
1 & \delta \tilde{\tau}_{s} \leq \tilde{t} < \tilde{\tau}_{s}, \\
1 - (\tilde{t} - \tilde{\tau}_{s})/\delta \tilde{\tau}_{s} & \tilde{\tau}_{s} \leq \tilde{t} < \tilde{\tau}_{s} + \delta \tilde{\tau}_{s}, \\
0 & \tilde{t} \geq \tilde{\tau}_{s} + \delta \tilde{\tau}_{s},
\end{cases} (6)$$

in which $\tilde{t} \equiv t - t_-$. The equation for \tilde{T} implies that the shear flow accelerates from zero to its maximum value over the ramping period $\delta \tilde{\tau}_s$, holds steady until $\tilde{t} = \tilde{\tau}_s$, and then decelerates until terminated at $\tilde{t} = \tilde{\tau}_s + \delta \tilde{\tau}_s$ [Fig. 2c]. The nearly negligible domain-averaged shear flow that may exist beyond the termination time in practice is then damped by replacing $\tilde{\mathbf{F}}_s$ with $-\langle \mathbf{u} \rangle_{xy}/\tilde{\tau}_{sd}$

until $t \equiv t_- + \tilde{t} = 0$. In the preceding expression for the damping rate, $\langle ... \rangle_{xy}$ has been used to denote the horizontal average of the bracketed variable. In general, the tilting procedure smoothly separates the lower vortex from the upper vortex over a transition layer between roughly 2.5 and 7.5 km above sea-level.

223 2c. Simulation Groups

222

224

The simulations conducted for this study can be separated into groups that are distinguished by 225 selected parameters used to prepare and force the system. The 8–16 simulations in any particular 226 group differ from one another only in the strength parameter a of the diabatic forcing [Eq. (1)], 227 which usually spans two orders of magnitude $[10^{-3} \text{ to } 10^{-1} \text{ K s}^{-1}]^2$ Variation of a over such 228 a broad interval will provide a thorough picture of how the vortex intensification process in 229 each simulation group changes with the magnitude of the low-level convergence generated by 230 the heating. A wide variety of simulation groups will be considered for the main purpose of demonstrating a certain universality of this picture. The differences between each simulation 232 group are explained below in the context of a reference group. 233

Table 1 lists all distinguishing or previously unspecified parameters related to the preparation and forcing of systems in the reference group. The vorticity coefficient ζ_o of the original vortex yields 235 winds of tropical storm intensity. The magnitude and duration of the preparatory shear flow are set 236 to leave the vortex with a core-scale tilt. Following a 6-h adjustment period after the preparatory shear flow subsides, at which point the clock reads t = 0, the tilt magnitude ($|\mathbf{x}_{ml,0}|$ in Table 1) is 238 81.8 km. By the same time, surface drag has reduced the maximum azimuthally averaged tangential 239 velocity in the boundary layer (v_{bm}) to 17.2 m s⁻¹, and the radius at which it occurs (r_{bm}) to 85.0 km. 240 Note that both v_{bm} and r_{bm} are measured in a polar coordinate system whose origin is at the lowlevel vortex center. The diabatic forcing of the vortex is peaked in the middle troposphere and is 242 minimal (but nonzero) at the surface. The heating distribution decays over a radial lengthscale of 243 35 km from its center \mathbf{x}_f in the horizontal plane. The heating center is driven toward its target location— the midlevel vortex center —on a time scale τ_f of 1 h. There is no sustained shear flow 245 to influence the intensification process that may commence when the diabatic forcing begins. 246

 $^{^2}$ The upper limit of a is extended to an unnaturally high value to provide a lucid picture of the scaling of the vortex intensification rate when the diabatic forcing is relatively strong; see section 4a for a related discussion.

Parameters	Values
Original Vortex $(t = t_{-})$	
$\zeta_o (10^{-4} \text{ s}^{-1})$	8.837
Preparatory Shear Flow $(t < 0)$	
$2U_s \text{ (m s}^{-1})$	8.3
t_{-} (h)	-12.0
$\delta ilde{ au}_{s}, ilde{ au}_{s}, ilde{ au}_{sd} ext{ (h)}$	1.0, 5.0, 1.5
Initial Vortex $(t = 0)$	
$\left \mathbf{x}_{ml,0}\right $ (km)	81.8
$v_{bm} (\mathrm{m s}^{-1})$	17.2
r_{bm} (km)	85.0
Diabatic Forcing	
$a ext{ (K s}^{-1})$	0.001-0.16
$z_f, \delta z_f^-, \delta z_f^+ \text{ (km)}$	7.5, 6.0, 3.5
δr_f (km)	35.0
$\delta au_f, au_f$ (h)	1.0, 1.0
$r_{f*}/ \mathbf{x}_{ml} $	1.0
$\varphi_{f*}(^{o})$	0.0
Sustained Shear Flow $(t > 0)$	
$2U_s \text{ (m s}^{-1})$	0.0

TABLE 1. Reference group parameters.

Table 2 lists all other simulation groups considered for this study, which differ from the reference 247 group by the parameter changes that are shown in the right-most column. Simulations in groups TLTX2 and TLTX3 are prepared with more intense preliminary shear flows that roughly double and 249 triple (respectively) the initial tilt magnitude. Simulations in group SH2P5∥ (SH2P5⊥) each include 250 sustained shear flows with $2U_s = 2.5 \text{ m s}^{-1}$ and $\hat{\mathbf{e}}_s$ rotated by an angle φ_e of 0^o (-90°) from the direction of the initial tilt vector $\mathbf{x}_{ml.0}$. In other words, the vortices in SH2P5|| (SH2P5 \perp) are exposed 252 to a modest level of shear parallel to (clockwise perpendicular to) the initial tilt. Simulations in 253 groups SH5 || and SH5 ⊥ are similar to those in their SH2P5-counterparts, except for having stronger 254 shear flows with $2U_s = 5 \text{ m s}^{-1}$. Simulations in group RFOUT are distinct from those in the reference group in having their heating centers shifted outward of the midlevel vortex center, by letting r_{f*} 256 equal 1.5 times the tilt magnitude. Simulations in groups PHIFM45 and PHIFP45 are distinct 257 in having their heating centers shifted 45-degrees clockwise and counterclockwise (respectively)

251

Group Name	Primary Distinction	Distinguishing Parameters
TLTX2	Initial tilt is roughly doubled.	Preparatory Shear Flow $(t < 0)$ $2U_S = 13.9 \text{ m s}^{-1}$ Initial Vortex $(t = 0)$ $ \mathbf{x}_{ml,0} = 146.8 \text{ km}$ $v_{bm} = 17.0 \text{ m s}^{-1}$ $r_{bm} = 87.5 \text{ km}$
TLTX3	Initial tilt is roughly tripled.	Preparatory Shear Flow $(t < 0)$ $2U_S = 19.4 \text{ m s}^{-1}$ Initial Vortex $(t = 0)$ $ \mathbf{x}_{ml,0} = 218.5 \text{ km}$ $v_{bm} = 16.7 \text{ m s}^{-1}$ $r_{bm} = 90.0 \text{ km}$
SH2P5	Weak sustained shear flow is added parallel to the initial $(t = 0)$ tilt vector.	Sustained Shear Flow $(t > 0)$ $2U_s = 2.5 \text{ m s}^{-1}$ $\varphi_e = 0^o$
SH2P5⊥	Weak sustained shear flow is added perpendicular to the initial ($t = 0$) tilt vector.	Sustained Shear Flow $(t > 0)$ $2U_s = 2.5 \text{ m s}^{-1}$ $\varphi_e = -90^o$
SH5	Moderate sustained shear flow is added parallel to the initial ($t = 0$) tilt vector.	Sustained Shear Flow $(t > 0)$ $2U_s = 5.0 \text{ m s}^{-1}$ $\varphi_e = 0^o$
SH5⊥	Moderate sustained shear flow is added perpendicular to the initial $(t = 0)$ tilt vector.	Sustained Shear Flow $(t > 0)$ $2U_s = 5.0 \text{ m s}^{-1}$ $\varphi_e = -90^o$
RFOUT	Center of diabatic forcing is shifted outward.	Diabatic Forcing $r_{f*} = 1.5 \mathbf{x}_{ml} $
PHIFM45	Center of diabatic forcing is shifted clockwise.	Diabatic Forcing $\varphi_{f*} = -45^o$
PHIFP45	Center of diabatic forcing is shifted counterclockwise.	Diabatic Forcing $\varphi_{f*} = 45^{o}$
ZFUP	Center of diabatic forcing is shifted upward.	Diabatic Forcing $z_f = 9.75 \text{ km}$
WEAKV	Initial vortex is weakened.	Original Vortex $(t = t_{-})$ $\zeta_{O} \rightarrow 5.302 \times 10^{-4} \text{ s}^{-1}$ Initial Vortex $(t = 0)$ $ \mathbf{x}_{ml,0} = 103.5 \text{ km}$ $v_{bm} = 11.4 \text{ m s}^{-1}$ $r_{bm} = 90.0 \text{ km}$
WEAKV-TLTX3	Initial vortex is weakened and the initial tilt is roughly tripled.	Original Vortex $(t = t_{-})$ $\zeta_O \rightarrow 5.302 \times 10^{-4} \text{ s}^{-1}$ Preparatory Shear Flow $(t < 0)$ $2U_s = 19.4 \text{ m s}^{-1}$ Initial Vortex $(t = 0)$ $ \mathbf{x}_{ml,0} = 249.8 \text{ km}$ $v_{bm} = 11.2 \text{ m s}^{-1}$ $r_{bm} = 90.0 \text{ km}$
CD0/CD0+	Surface drag is eliminated/reduced.	$C_d \to 0/2.5 \times 10^{-5}$

TABLE 2. Features distinguishing the non-reference groups from the reference group.

from the direction of the tilt vector. Simulations in group ZFUP distinctly have their altitudes of maximal heating shifted 2.25 km upward. Simulations in group WEAKV have relatively weak original vortices, characterized by a 40% reduction of ζ_o . Simulations in group WEAKV-TLTX3 are similar to those in WEAKV, but their initial vortices have much larger tilts.

The final two simulation groups listed in Table 2 (CD0 and CD0+) have drastic reductions of surface drag. CD0 changes the bottom surface boundary condition to free-slip, whereas CD0+ homogenizes and reduces C_d by two orders of magnitude. Comparison of these simulation groups to the reference group (henceforth labeled REF in tables and figures) will illustrate a sharp distinction between weakly forced simulations with negligible and standard levels of surface drag.³ A more comprehensive analysis of how results vary with the surface drag parameterization would stray too far from the main narrative of this paper, but is provided in appendix B for readers who may have some interest in the topic. Note that appendix B is best read after section 3.

3. Simulation Results

3a. Variation of the Intensification Time Scale with the Heating Magnitude

263

264

266

267

269

270

271

273

274

Figure 4 illustrates how the time t_2 required for v_{bm} to double varies with the magnitude 276 a of the diabatic forcing in the reference group (black diamonds). The doubling period is 277 normalized to a certain time scale τ_{σ} that increases with decreasing a (inset). Specifically, τ_{σ} is the inverse of the mean boundary layer convergence in the neighborhood of the diabatic forcing. 279 The aforementioned boundary layer convergence is defined by $\sigma_b \equiv -\nabla_H \cdot \mathbf{u}_b$, in which ∇_H is the 280 horizontal gradient operator, and \mathbf{u}_b is the vertical average of \mathbf{u} over the lowest 1.2 km of the 281 troposphere.⁴ The computation of au_{σ} generally involves taking the spatial average of σ_b over a circular disc of radius δr_f centered at \mathbf{x}_f , where the applied heating is maximized in the horizontal 283 plane. Using the divergence theorem, the disc average can be written $\sigma_{bf} = -2u_{bf}/\delta r_f$, in which 284 u_{bf} is the azimuthally averaged radial component of \mathbf{u}_b (in a coordinate system centered at \mathbf{x}_f)

³Data from *both* CD0 and CD0+ are considered to verify that negligible-drag results are insensitive to minor differences in the CM1 configuration options that are used in conjunction with free-slip and semi-slip boundary conditions.

⁴This definition of the horizontal boundary layer velocity field is also used to evaluate the maximum wind speed v_{bm} that was introduced in section 2c.

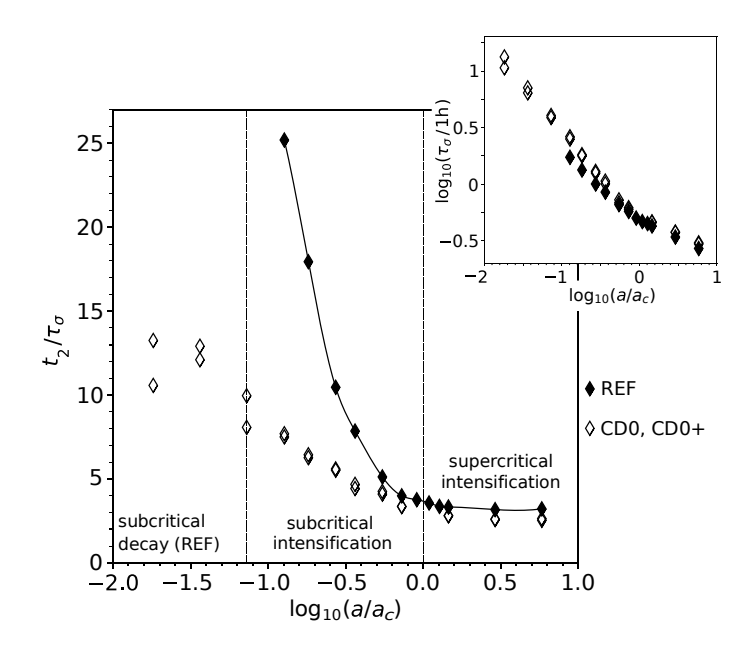


Fig. 4: Main plot: Normalized length of time required for v_{bm} to double versus the normalized heating magnitude in the reference group (black diamonds) and in similar simulations with the surface drag severely reduced or eliminated (white diamonds). The dashed vertical lines at (left) $a = a_0$ and (right) $a = a_c$ mark the boundaries between the domains of (left to right) spindown, subcritical intensification, and supercritical intensification in the reference group. Inset: Anticorrelation between the convergence time scale (in the vicinity of diabatic forcing) and the heating magnitude.

along the periphery of the disc. For the present analysis, the computation of τ_{σ} also involves taking a time average of σ_{bf} that begins at $t_{\alpha} = 0$ and extends to $t_{\beta} = t_2$. To summarize,

288

292

293

295

296

$$\tau_{\sigma} \equiv -(t_{\beta} - t_{\alpha}) / \int_{t_{\alpha}}^{t_{\beta}} \frac{2u_{bf}}{\delta r_{f}} dt . \tag{7}$$

Fundamentally, τ_{σ} is a characteristic time scale for horizontal fluid contraction near the surface in the vicinity of the diabatic forcing. One may also view τ_{σ} as the time scale for the amplification of vertical vorticity resulting from such contraction.

The data in Fig. 4 show that when the heating magnitude a exceeds a critical value, given by $a_c \approx 0.0275 \text{ K s}^{-1}$, the normalized intensification time scale t_2/τ_σ has a nearly constant value between 3 and 4. In other words, the v_{bm} -doubling period is directly proportional to τ_σ . Below the critical value, t_2/τ_σ rapidly grows and diverges as a decreases toward $a_0 \approx 0.002 \text{ K s}^{-1}$ (left dashed line). The divergence reflects diabatic spinup diminishing to the point of becoming completely countered by the negative impact of surface drag (see section 3d.3). For $a < a_0$, the vortex decays.

Although surface friction markedly exacerbates the subcritical slowdown of intensification, 298 there is clear evidence that the normalized growth of t_2 with decreasing a (below a_c) has other 299 contributing factors. The white diamonds superimposed on Fig. 4— taken from groups CD0 300 and CD0+ —show that removing surface friction from the reference group does not eliminate Although t_2 no longer diverges as a approaches a_0 from the right, subcritical slowdown. 302 decreasing a from a_c toward zero still causes multifold growth of t_2/τ_{σ} . In other words, a less 303 efficient intensification mechanism appears to emerge as a drops below a_c regardless of whether 304 the simulation includes surface drag. 305

3b. Subcritical and Supercritical Pathways of Intensification

306

307

308

Figure 5 illustrates the root cause for the dynamical transition across the critical heating 309 magnitude a_c . Each panel shows near-surface streamlines superimposed over a contour plot of 310 relative vertical vorticity ζ in a pertinent subregion of the low-level vortex near the center of the diabatic forcing, immediately or soon after the forcing reaches full strength. The images are in a 312 reference frame that moves with the heating center, in which the horizontal velocity field is given by 313 $\tilde{\mathbf{u}} \equiv \mathbf{u} - d\mathbf{x}_f/dt$. Each column corresponds to a distinct simulation from the reference group, with a increasing from left to right. The heating rates of the left and middle simulations are subcritical, 315 whereas that of the right simulation is supercritical. Both subcritical cases show confluence of 316 streamlines with peak convergence somewhat downstream of \mathbf{x}_f . The confluence coincides with 317 amplification of vertical vorticity, but the fluid which carries the enhanced vorticity (and remains 318 near the surface) eventually leaves the convergence zone to potentially recirculate around the 319 broader cyclone. When the heating rate is supercritical, the streamlines develop a point of attraction 320 inside the convergence zone. The bulk of fluid entering the convergence zone cannot escape in the horizontal plane, and the vorticity of that which remains near the surface continuously amplifies. 322 Figures 6-8 provide broader perspectives of the near-surface vorticity evolution and wind speed 323 intensification in each of the foregoing simulations, as viewed from an earth-stationary reference frame. Figure 6 corresponds to the subcritical system subjected to the weakest forcing. The escape 325 of enhanced vorticity from the convergence zone and its subsequent recirculation are evident upon 326

comparing the ζ -snapshots at t = 1.5 and 4 h. As the system evolves, the distance between the

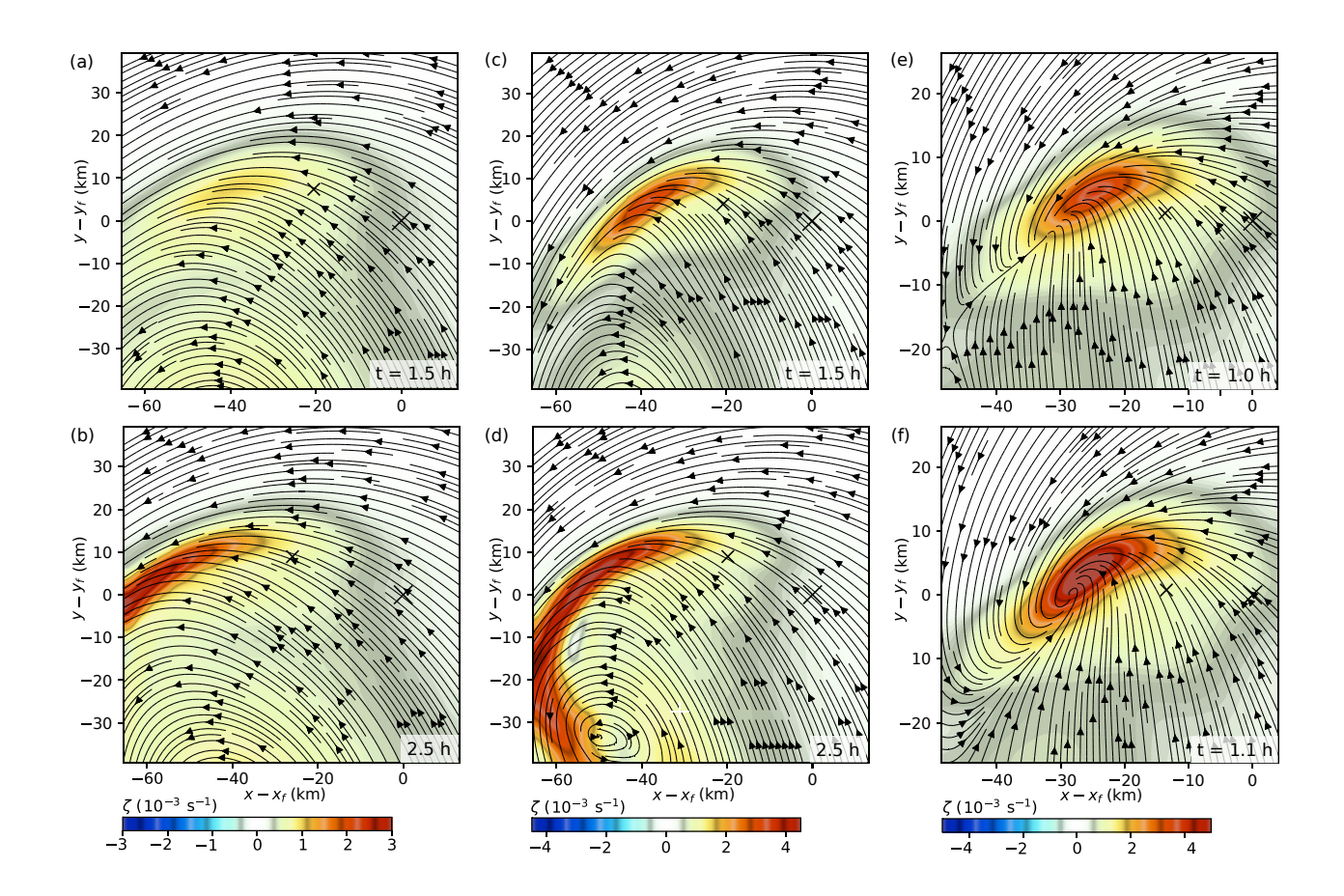


Fig. 5: (a) Horizontal streamlines superimposed over relative vorticity ζ at z = 0.7 km and t = 1.5 h in the reference group simulation with $a = 2a_c/11$. The streamlines are in a reference frame that moves with the heating center. The big (little) \times is located at the heating center \mathbf{x}_f (convergence center \mathbf{x}_σ , defined in appendix A). (b) As in (a) but at t = 2.5 h. (c,d) As in (a,b) but for the reference group simulation with $a = 4a_c/11$. (e,f) As in (a,b) but for the reference group simulation with $a = 12a_c/11$, and at (e) t = 1.0 h and (f) t = 1.1 h.

low-level vortex center (white +) and the heating center (large black ×) decays at a variable rate. 328 Henceforth, this distance will be represented by the variable $\ell \equiv |\mathbf{x}_f - \mathbf{x}_\ell|$. As ℓ progressively decays, 329 the radius of maximum wind speed contracts and the vortex intensifies. The process resembles that found for the shallow-water vortices forced by stationary or slowly precessing subcritical mass sinks in S20. One caveat is that the location of the diabatic forcing (analogous to the mass 332 sink) in the present simulation is explicitly linked to the location of the midlevel vortex center. 333 Therefore—unlike a shallow-water system —the reduction of ℓ over time (indicating alignment) involves both low-level and midlevel vortex dynamics. 335

331

336

Figure 7 corresponds to the subcritical system with intermediate forcing. Although the nearsurface streamlines do not develop a point of attraction in the vicinity of the heating center, the

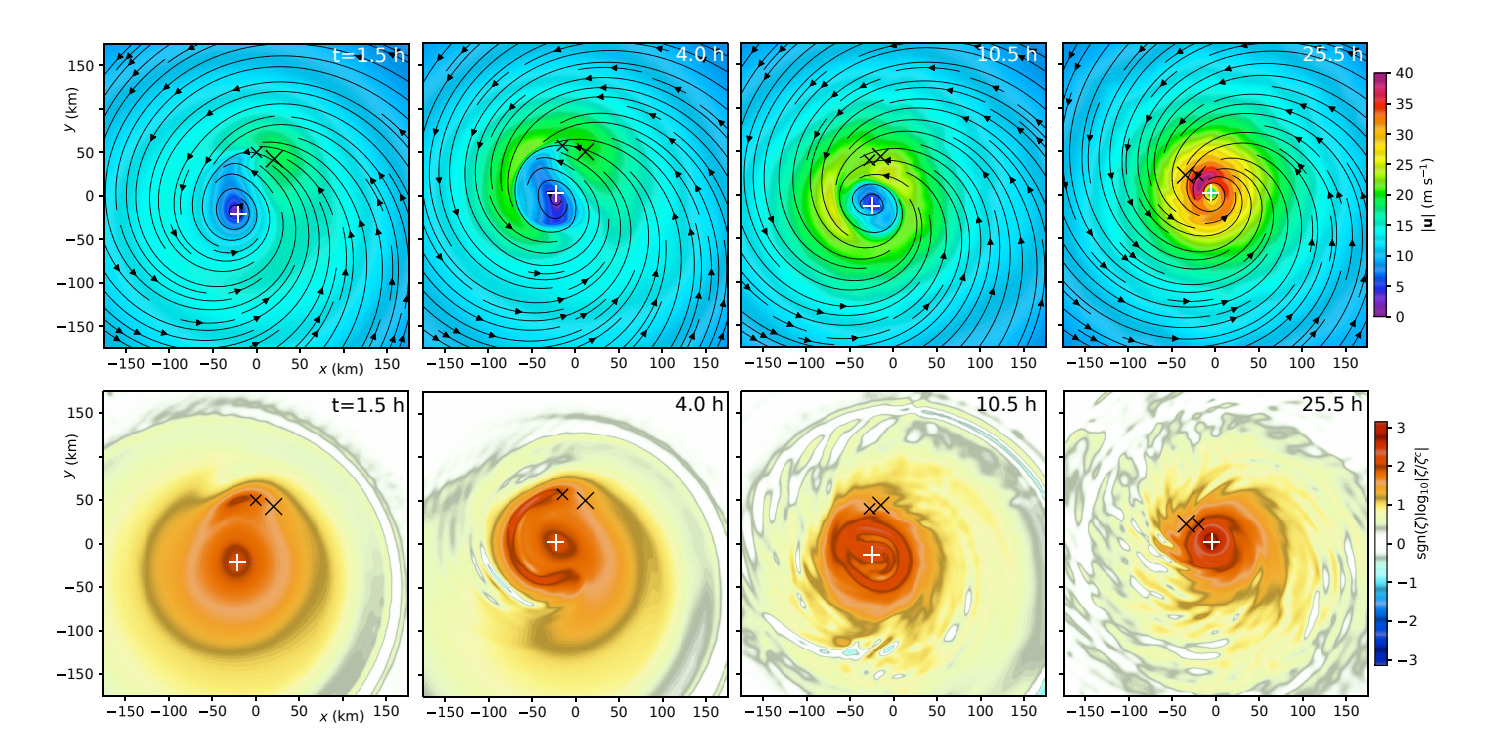


Fig. 6: Subcritical vortex intensification in the reference simulation with $a=2a_c/11$, viewed in an earth-stationary reference frame with a domain-centered coordinate system. Top row (left to right): sequential snapshots of the streamlines and magnitude of the horizontal velocity field \mathbf{u} at z=50 m. Bottom row: corresponding sequential snapshots of relative vertical vorticity ζ (normalized to $\zeta^c=10^{-5}~{\rm s}^{-1}$) at z=0.7 km, displayed using a logarithmic colormap for all grid-cells with $\log_{10}|\zeta/\zeta^c| \geq 0$. Grid-cells with $\log_{10}|\zeta/\zeta^c| < 0$ are white. In all plots, the large (small) \times is located at the heating center (convergence center). The white + is located at the low-level vortex center.

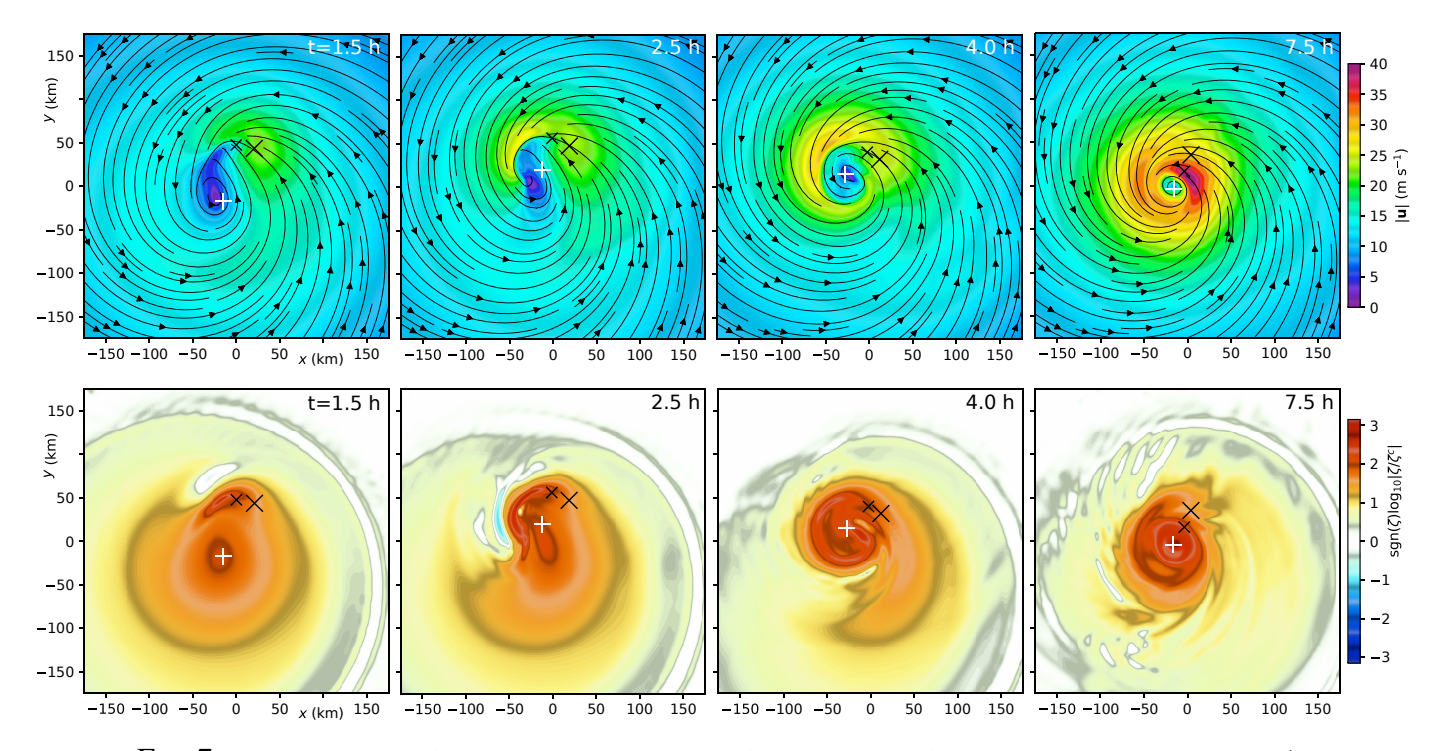


Fig. 7: As in Fig. 6, but for subcritical vortex intensification in the reference simulation with $a = 4a_c/11$.

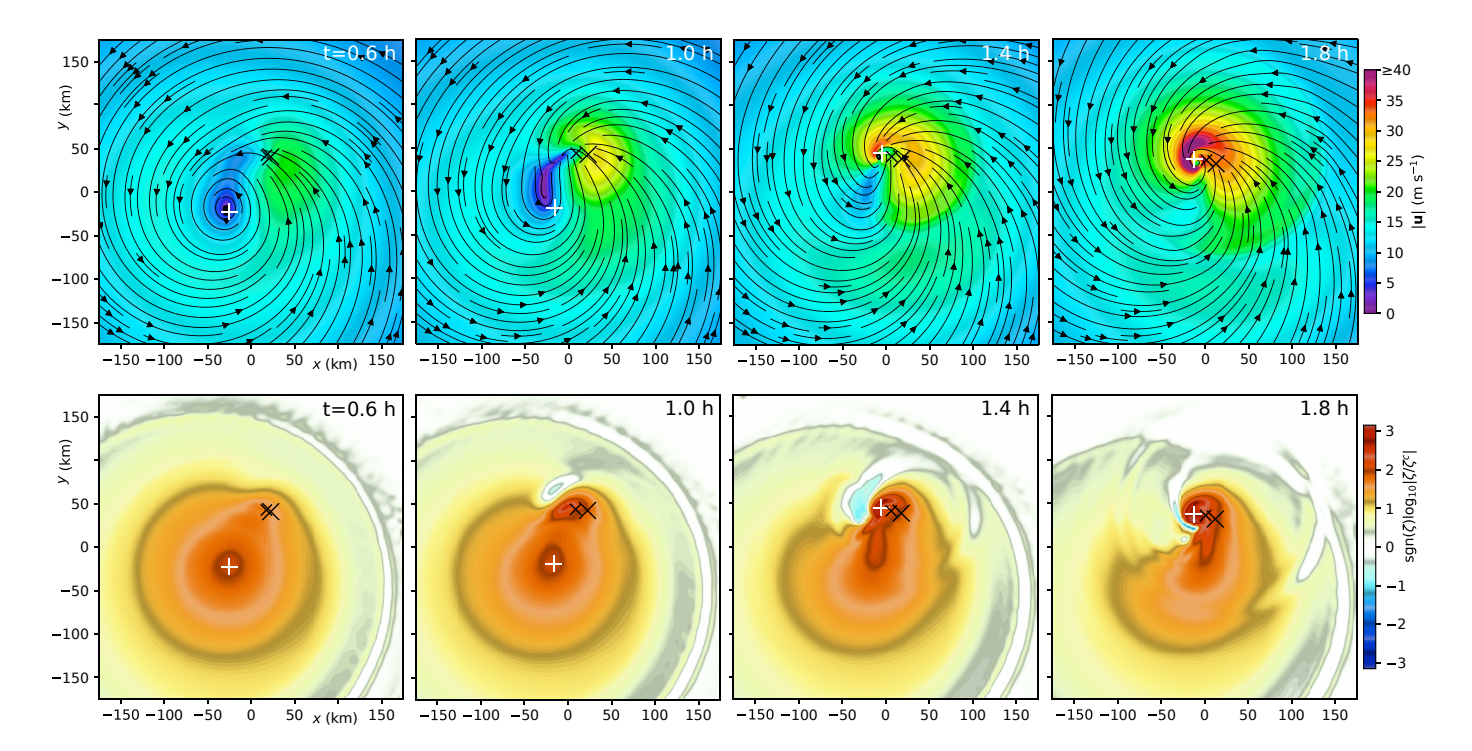


Fig. 8: As in Fig. 6, but for supercritical vortex intensification in the reference simulation with $a = 12a_c/11$.

streamer of enhanced vorticity leaving the area does not travel too far away. Instead, the head of the streamer shortly coalesces with the central vorticity anomaly of the original cyclone as the latter surges closer to \mathbf{x}_f . The end result is a smaller vortex core whose center lies closer to the diabatic forcing. Whether the depicted evolution should be viewed as a variant of "core reformation" will be discussed shortly.

Figure 8 corresponds to the supercritical system subjected to the strongest forcing. The near-surface streamlines are seen here, as in Fig. 5e, to have formed a point of attraction near \mathbf{x}_f after an hour of development, at which time the diabatic forcing has achieved full intensity. Immediately afterward— within a period that is appreciably shorter than the advective time scale over a distance comparable to ℓ —the low-level vortex center jumps to \mathbf{x}_f , where an intensifying subvortex becomes dominant over a lengthscale comparable to that of a typical hurricane eyewall. For reasons to be clarified below, the depicted evolution will be considered a proper case of "core replacement." The subsequent intensification is unnaturally fast for a tropical cyclone, suggesting that the diabatic forcing is either unnaturally strong or would not persist for more than a brief moment in reality. Section 4a will reexamine this issue more quantitatively, and put forth theoretically realizable conditions for which supercritical intensification following core replacement may operate over a longer time scale (in units of hours) under weaker forcing.

Figure 9 shows time series of several notable vortex parameters in each of the preceding sim-355 ulations. The vortex parameters include v_{bm} , r_{bm} , the radial offset ℓ of the diabatic forcing, and 356 an alternative measure of the aforementioned offset given by $\ell_2 \equiv |\mathbf{x}_f - \mathbf{x}_{l2}|$. Whereas \mathbf{x}_l (in the 357 definition of ℓ provided earlier) represents the low-level vortex center viewed on radial scales exceeding 10 km, \mathbf{x}_{l2} represents the low-level vortex center viewed on radial scales exceeding 70 km, 359 which is comparable to the original core size (see appendix A). Note that the values of v_{bm} and 360 r_{bm} shown here and elsewhere are obtained from a search over the boundary layer vortex that is restricted to $r \ge 10$ km, in part to ensure that the maximum wind speed measurement pertains to 362 a well-resolved structure. The 10-km cut-off is judged to be acceptable for this study, because 363 intensifying tropical cyclones do not usually have smaller values of r_{bm} while at the strength of a tropical storm or low-category hurricane [e.g., Kimball and Mulekar 2004]. 365

Let us first consider the time series for the subcritical simulations. Figure 9a corresponds to the 366 simulation having the weakest diabatic forcing. The initial values of r_{bm} , ℓ and ℓ_2 are virtually 367 equivalent. After the 1-h ramping of the heat source, the vortex undergoes a 2-h adjustment to a state in which the aforementioned lengthscales have dropped by approximately thirty percent. 369 Subsequently, r_{bm} steadily decays and v_{bm} continuously grows. Although ℓ and ℓ_2 eventually 370 decay toward the r_{bm} curve, the onsets of their decays are delayed. Figure 9b corresponds to the simulation having intermediate forcing. The early contractions of the radial lengthscales are more 372 pronounced, and those of ℓ and ℓ_2 are not as uniform. Furthermore, the time scale of the dynamics 373 is shorter whether viewed in units of hours or τ_{σ} . Otherwise, the plotted time series do not radically differ from those of the other subcritical system with relatively weak forcing. 375

Figure 9c corresponds to the supercritical simulation. In contrast to the preceding cases, the early drops of r_{bm} and ℓ are virtually discontinuous (occurring almost entirely over an interval shorter than τ_{σ}) and terminate at lengths appreciably smaller than δr_f . The discontinuous drops of r_{bm} and ℓ occur once the tangential wind speed of the small-scale vortex emerging in the vicinity of diabatic forcing exceeds that of the large-scale parent cyclone, and \mathbf{x}_l immediately jumps to a location inside the forcing region. During this jump, the large-scale vortex center \mathbf{x}_{l2} essentially holds position. Over time, the large-scale center gradually rejoins the small-scale center, through a process that presumably involves the continual convergence of outer absolute vorticity toward \mathbf{x}_l combined with axisymmetrization mechanisms similar to those found in nondivergent vortices.

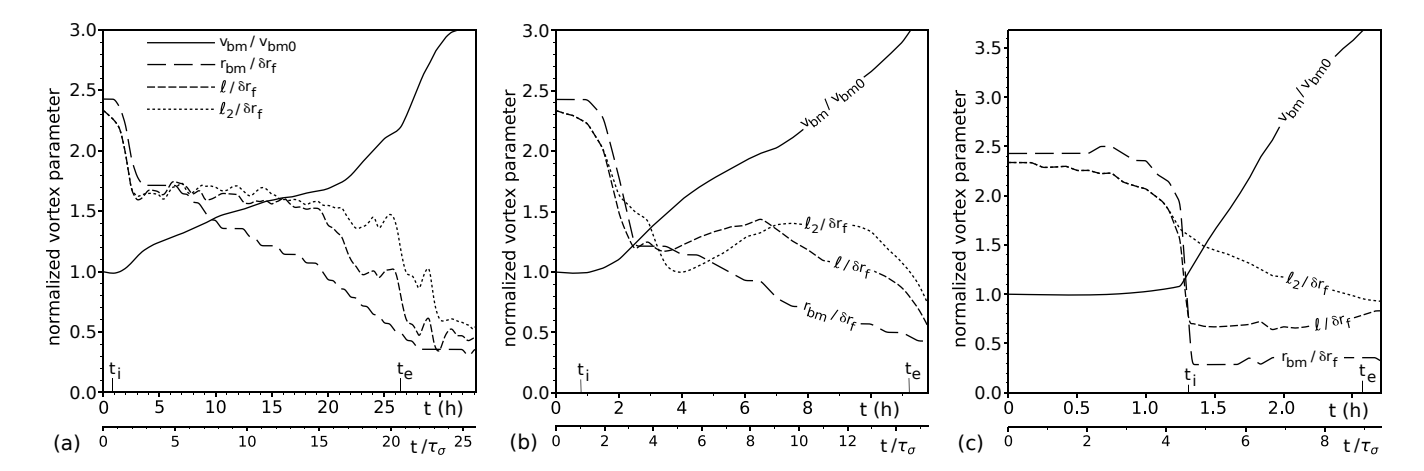


Fig. 9: (a) Time series of (solid) the maximum tangential velocity in the boundary layer v_{bm} , (long-dashed) the radius of maximum velocity in the boundary layer r_{bm} , (short-dashed) the distance ℓ from the heating center to the principal low-level vortex center \mathbf{x}_l , and (dotted) the distance ℓ_2 from the heating center to the large-scale low-level vortex center \mathbf{x}_{l2} , for the subcritical reference simulation with $a = 2a_c/11$. The plotted values of v_{bm} are normalized to the initial value v_{bm0} , whereas the plotted values of r_{bm} , ℓ and ℓ_2 are normalized to the radial lengthscale of the heating distribution δr_f . The secondary time axis shows t normalized to τ_{σ} defined with the averaging of σ_{bf} between t_i and t_e (see section 3d.1), which are marked on the bottom of the plot. (b) As in (a) but for the subcritical reference simulation with $a = 4a_c/11$. (c) As in (a) but for the supercritical reference simulation with $a = 12a_c/11$.

The major discontinuous separation and subsequent convergence of \mathbf{x}_l and \mathbf{x}_{l2} are reflected in the major discontinuous splitting and gradual rejoining of ℓ and ℓ_2 .

3c. Core Reformation and Core Replacement

388

389

391

392

394

The term "core (or center) reformation" is widely used in tropical cyclone meteorology in reference to the occasionally observed rapid emergence of a relatively small but dominant vorticity core in an area of localized convection away from the original center of a pre-hurricane vortex [e.g., Molinari et el. 2004; Molinari and Vollaro 2010; Nguyen and Molinari 2015; Chen et al. 2018; Alvey et al. 2022]. This fairly broad concept might be seen to encompass the initial phases of the intensification processes in both the subcritical system with intermediate forcing⁵ and the supercritical system considered in section 3b. Nevertheless, the core reformation mechanisms

⁵There are several reasons why the subcritical dynamics of the system with $a=4a_c/11$ might be seen to entail a marginal case of core reformation. As shown earlier, the vortex core in the boundary layer rapidly (over a period of 1.5 hours) shrinks to one-half of its initial size in terms of r_{bm} , while relocating to a position substantially closer to the diabatic forcing. Immediately after this event, the centers of the small new core and the broader circulation linked to the original core are arguably well separated. [The measured separation distance ranges from 24 to 50 km when the defining radial lengthscale of the broader circulation (r_c of appendix A) is between 70 and 100 km.] Furthermore, the subsequent wrapping of outer vorticity around the new core [Fig. 7, t=4 h] resembles the aftermath of a prototypical reformation event illustrated in Fig. 11 of Molinari et al. [2004].

differ between the two cases. Most notably, the supercritical mechanism distinctly entails the appearance of a point of attraction for the streamlines in close proximity to the heating center, where the convergence of trapped fluid generates a new core with a lengthscale considerably smaller than δr_f . To avoid ambiguity in terminology, the supercritical mode of core reformation will be called "core replacement".⁶

S20 derived a theoretical condition for the early existence of the point of attraction required to initiate core replacement. With a few simplifying assumptions, a point of attraction was found to exist in the convergence zone generated by diabatic forcing *iff*

402

405

413

422

$$\frac{\tau_c}{\tau_c} > 1. \tag{8}$$

In the preceding condition, τ_c is the time required for the local background flow to advect a fluid parcel across one-half the radial lengthscale of the convergence zone in a reference frame moving with the translational velocity of the convergence zone, and (as before) τ_{σ} is the local time scale for horizontal fluid contraction. We hypothesize that condition (8) applies not only to the shallow-water systems of S20, but is also required for core replacement in the three-dimensional systems under present consideration if τ_{σ} and τ_c are appropriately calculated. The formula for τ_{σ} will be given by Eq. (7). The formula for τ_c will be given by

$$\tau_c \equiv (t_{\beta} - t_{\alpha}) / \int_{t_{\alpha}}^{t_{\beta}} \frac{2 \left| \mathbf{u}_c - d\mathbf{x}_f / dt \right|}{\delta r_f} dt , \qquad (9)$$

in which $\mathbf{u}_c \equiv \bar{v}_{b2}\hat{\varphi}_2 + \langle \mathbf{u}_b \rangle_{xy}$, \bar{v}_{b2} is the azimuthal mean tangential component of \mathbf{u}_b evaluated at the radius ℓ_2 in a polar coordinate system centered at \mathbf{x}_{l2} , $\hat{\varphi}_2$ is the azimuthal unit vector at \mathbf{x}_f in the same coordinate system, and $\langle \mathbf{u}_b \rangle_{xy}$ is the domain average of \mathbf{u}_b . In the preceding formulation, \mathbf{u}_c neglects the presumably subdominant radial $(\hat{\mathbf{r}}_2)$ velocity field of the large-scale cyclone, but keeps $\langle \mathbf{u}_b \rangle_{xy}$ owing to its potential importance in simulations with a substantial environmental shear flow. The end points of the time-averaging intervals $(t_\alpha$ and $t_\beta)$ used to evaluate τ_σ and τ_c must of course be chosen to have relevance for the intensification period under consideration, and will be specified below.

⁶In S20, the author reserved the term "core reformation" for its supercritical variant ("core replacement"). In hindsight, this may have been too restrictive.

3d. Comprehensive Analysis of the Intensification Rate

424

430

432

434

Heretofore, the focus has been on simulations from the reference group. The present goal is to demonstrate the similarity between intensification in the reference group and in all other simulations having the standard parameterization of oceanic surface drag. Rather than revisit the v_{bm} -doubling period, which does not exist when a vortex decays, the new focus will be on the intensification rate (IR) given by

$$\frac{\delta v_{bm}}{\delta t} \equiv \frac{v_{bm}(t_e) - v_{bm}(t_i)}{t_e - t_i},\tag{10}$$

in which t_i and t_e are the start and end times of a judiciously chosen intensification period.

3d.1 Boundaries of the Intensification Period

The default and most common value for t_i is set to $t_{id} \equiv 0.8$ h, which corresponds to 435 when the diabatic forcing has achieved 80 percent of its ultimate strength. A modification is made if a signature of core replacement is observed after t_{id} . Specifically, t_i is reset to when the ratio 437 of ℓ to ℓ_2 (which starts at 1) is first seen to have precipitously fallen to a value less than 0.45. 438 For all applicable simulations considered herein, this event coincides with virtually discontinuous 439 drops of r_{bm} and ℓ to values comparable to δr_f or smaller. The foregoing reset of t_i guarantees that the measured IR starts promptly after core replacement. Modifications to t_i are also made 441 for simulations in groups TLTX2, TLTX3, RFOUT, WEAKV and WEAKV-TLTX3 that do not 442 involve core replacements. Simulations from the aforementioned groups differ from others in having ℓ initially greater—sometimes much greater—than r_{bm} . After an adjustment period, the 444 time series of ℓ and r_{bm} converge so as to better resemble the states of their counterparts from 445 other groups at $t = t_i$. Accordingly, should the event occur after t_{id} , the start time t_i is reset to when the ratio of ℓ to r_{bm} drops below 1.05. 447 The default end time t_e is the solution of the following equation: $t_e = t_i + 20\tau_{\sigma}^{ie}$, in which τ_{σ}^{ie} is 448 given by the right-hand side of Eq. (7) with $t_{\alpha} = t_i$ and $t_{\beta} = t_e$. If the time t_3 at which v_{bm} becomes 449 three-times larger than its value at t_i is smaller than the default end time, the end time is reset to t_3 .

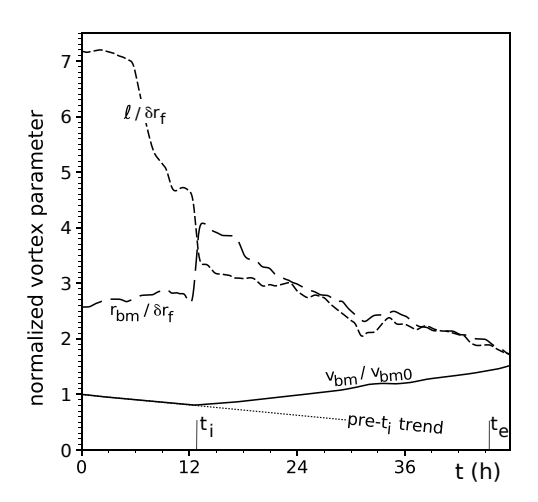


Fig. 10: As in each subplot of Fig. 9, but for a simulation from group WEAKV-TLTX3 with a = 0.0035 K s⁻¹; ℓ_2 is excluded from the plot because of its near equivalence to ℓ . The dotted line is an imaginary extension of the decay trend for v_{bm} seen prior to t_i .

This reset generally prevents the intensification interval from overlapping the final phase of vortex development that is characterized by steady v_{bm} .

The beginning and end of the intensification period of each reference simulation in Fig. 9 are 453 marked by the ticks labeled t_i and t_e on the bottom axis of each subplot. These examples are 454 considered typical for systems with [Fig. 9c] and without [Figs. 9a and 9b] a core replacement 455 event. Figure 10 is similar to an individual subplot of Fig. 9, but for an illustrative simulation from 456 WEAKV-TLTX3 that intensifies without undergoing core replacement. Here the initial adjustment preceding t_i involves a roughly fifty-percent reduction of ℓ and a roughly fifty-percent growth of 458 r_{bm} . Note that while ℓ at the start of the intensification period may be smaller than its initial 459 value, it is still considerably larger than ℓ at t_i in comparable reference simulations [e.g., Fig. 9a]. Forthcoming analysis [the inset of Fig. 14a] will show the same to be true for all simulations devoid 461 of core replacement events in WEAKV-TLTX3 and other groups (TLTX2 and TLTX3) whose 462 constituent systems are initialized with relatively large tilts. 463

The reader may have some concern that— for systems with applied shear —the orientation of the tilt vector relative to $\hat{\mathbf{e}}_s$ during the intensification period $(t_i \le t \le t_e)$ differs considerably from its initial setting, which would render that initial setting irrelevant. For subcritical systems, the time-averaged angle between the tilt vector and $\hat{\mathbf{e}}_s$ ($-\varphi_e$) during the intensification period is $15.3 \pm 31.8^\circ$ for SH2P5||, $68.2 \pm 19.2^\circ$ for SH2P5 \perp , $8.5 \pm 16.3^\circ$ for SH5||, and $49.3 \pm 8.3^\circ$ for SH5 \perp . Here, each angle is given as a group mean \pm one standard deviation. The preceding measurements suggest that while the shear-relative tilt angles in SH2P5|| and SH2P5 \perp (or SH5||

and SH5 \perp) are somewhat closer to each other than initially intended, the difference generally remains pronounced during the intensification period. For supercritical systems, the intensification period starts after core replacement creates an aligned vortex that rapidly intensifies and becomes virtually immune to moderate shearing. The author has difficulty imagining how at this point the orientation of the minimal tilt vector could be important.

3d.2 Similarity of the IR Curves

476

478

496

498

499

Figure 11 shows the dependence of a nondimensional measure of the IR on a criticality 479 parameter that can be viewed as a nondimensional measure of the strength of diabatic forcing. The 480 nondimensional IR is given by $(\delta v_{bm}/\delta t) \times \tau_{\sigma}^{ie}/v_i$. The velocity that appears in the denominator 481 of the scaling factor is defined by $v_i \equiv (3\delta r_f/2) \iint_A d^2\mathbf{x} [\zeta_b(\mathbf{x}, t_i) + f]/A$, in which $\zeta_b \equiv \hat{\mathbf{z}} \cdot \nabla_H \times \mathbf{u}_b$ 482 and the integral is over the area A of a circular disc of radius $3\delta r_f$ centered at $\mathbf{x}_f(t_i)$. Use of 483 the preceding scaling velocity helps reduce the IR-spread in systems having the same criticality parameter but different vortex strengths or forcing locations at the start of intensification.⁷ The 485 criticality parameter is defined by the ratio τ_c/τ_σ^{ie} [cf. Eq. (8)], in which the time scale τ_c for 486 advection across the forcing region is given by Eq. (9) with $t_{\alpha} = t_i$ and $t_{\beta} = t_i + (t_e - t_i)/3$. Note that the averaging interval used to compute τ_c is confined to an early phase of intensification. 488 Extending the interval to a later phase—when ℓ_2 is smaller and the vortex is stronger—could 489 substantially decrease the value of the criticality parameter. The time scale τ_{σ} for convergence in the neighborhood of the steady diabatic forcing is generally less sensitive to the end-point t_{β} used 491 for its evaluation. Appendix C tabulates basic statistics for v_i and τ_c for the simulations under 492 present consideration. The fractional variations of v_i and τ_c within a given simulation group are 493 generally small compared to those of τ_{σ} , but their characteristic values may differ considerably between two simulation groups. 495

Each simulation group in Fig. 11 is represented by a symbol with a distinct combination of size, shape and color (see the legend). Filled symbols with the darkest shading correspond to simulations that undergo robust core replacements. Consistent with theoretical expectations, these simulations generally have criticality parameters exceeding unity. The empty (white filled) symbols correspond

⁷The alternative use of $v_{bm}(t_i)$ is found to less effectively reduce the spread.

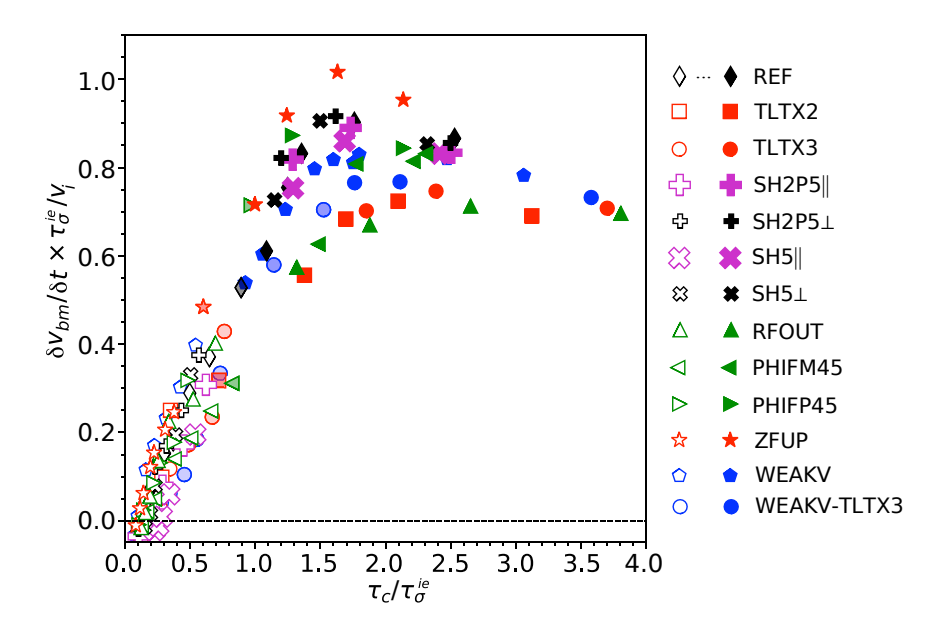


Fig. 11: Nondimensional IR plotted against the criticality parameter for all simulations with standard oceanic surface drag. See section 3d.2 for details.

to simulations that show no sign of core replacement during vortex intensification. Consistent with theoretical expectations, these simulations have criticality parameters less than unity.

However, the boundary between simulations with and without core replacement appears to be less sharp than theory would suggest. A small number of simulations with criticality parameters measurably less than unity (whose symbols have relatively light shading) were flagged by an objective algorithm for exhibiting core replacement. The algorithm does not explicitly check for a point of attraction in the vicinity of diabatic forcing, but does check for a pronounced splitting of small-scale and large-scale vortex centers, coinciding with discontinuous drops of r_{bm} and ℓ to values comparable to δr_f or smaller. In some cases (symbols with the lightest shading) the small-scale core quickly escapes the forcing region and weakens relative to the large-scale circulation so as to revert into a subdominant subvortex. The preceding scenario generally coincides with ℓ becoming greater than $2\delta r_f$. In other cases (symbols with medium shading) there is no sign of the small-scale core returning to subdominant status, but its center at some point in time obtains a position where $\delta r_f < \ell < 2\delta r_f$. Similar behavior was also seen in two WEAKV-TLTX3 simulations with criticality parameters measurably greater than unity. By contrast, ℓ promptly becomes and remains smaller than δr_f after core replacement in the multitude of all other (darkly shaded) supercritical simulations.

In the supercritical parameter regime where all measures indicate that core replacement gen-517 erally occurs and is nearly always robust, the normalized IR can be viewed to have an approx-518 imately constant value of 0.8 ± 0.1 . In the subcritical parameter regime, the variation of the 519 normalized IR in each simulation group can be approximated by a linear expression of the form $\mu[\tau_c/\tau_\sigma^{ie}-(\tau_c/\tau_\sigma^{ie})_0]$. Linear regressions for data with $\tau_c/\tau_\sigma^{ie}<0.9$ give slopes and points of zero 521 IR of $\mu = 0.73 \pm 0.13$ and $(\tau_c/\tau_\sigma)_0 = 0.15 \pm 0.06$, respectively. Here, each parameter is expressed 522 as a mean ± one standard deviation of the results obtained for each simulation group. Pearson correlation coefficients close to unity (0.983 ± 0.021) verify that the linear model is generally 524 an appropriate working assumption.⁸ 525

In the supercritical parameter regime, the combination of roughly constant values for the normalized IR and v_i [Table C1] in a given simulation group implies that $\delta v_{bm}/\delta t \approx c_g/\tau_\sigma^{ie}$ following a core replacement event, in which c_g is a group-specific constant. This means that to a good approximation, the dimensional IR is directly proportional to the boundary layer convergence in the vicinity of the diabatic forcing. In the subcritical parameter regime, the IR scaling factor is normally well described by a relation of the form $\tau_\sigma^{ie}/v_i \propto (\tau_\sigma^{ie}/\tau_c)^\chi$, in which $\chi = 1.1 \pm 0.1$ according to linear regressions of log-transformed data for each simulation group. It follows that for the data considered herein, one might reasonably approximate the subcritical variation of dimensional IR with the criticality parameter by the nonlinear relation $\delta v_{bm}/\delta t \approx k_g(\tau_c/\tau_\sigma^{ie})[(\tau_c/\tau_\sigma^{ie})-(\tau_c/\tau_\sigma^{ie})_0]$, in which k_g is a group-specific constant and χ has been set to unity.

3d.3 Sawyer-Eliassen Based Analysis of Low-Level Spinup

526

527

528

529

531

532

534

535

537

538

539

540

Section 3a suggested that the growth of the nondimensional intensification rate from the point of zero IR to supercriticality is not exclusively a consequence of frictional damping becoming less effective in counteracting the growing strength of diabatic forcing. Nevertheless, the diminishing

 $^{^8}$ A sensitivity test has been conducted with τ_σ redefined to be the inverse of the average of σ_b within a radius δr_f of the convergence center \mathbf{x}_σ that is precisely defined in appendix A; for supercritical (subcritical) systems, the average of $|\mathbf{x}_\sigma - \mathbf{x}_f|/\delta r_f$ over the intensification period is 0.23 ± 0.03 (0.66 ± 0.11). The redefinition typically results in a moderate fractional reduction of τ_σ^{ie} for subcritical systems. The correlation coefficient between the normalized IR and τ_c/τ_σ^{ie} remains high (0.963 ± 0.020) in the realm of subcriticality, but the spread of the point of zero IR (0.18 ± 0.12) becomes noticeably greater. The value of τ_c/τ_σ^{ie} separating systems with robust core replacements from those without increases to a value slightly closer to 1.

 $^{^9}$ Group TLTX3 is excluded from the stated mean and standard deviation of χ . The regression for TLTX3 (which yields $\chi=0.67$) has a correlation coefficient of 0.588, indicating a poor fit. For the other simulation groups, the correlation coefficient is 0.986 ± 0.015 .

importance of frictional damping is a major factor contributing to accelerated spinup that merits further discussion. Such discussion is facilitated by using the traditional framework of Sawyer-Eliassen (SE) theory [Shapiro and Willoughby 1982; Schubert and Hack 1982; Smith et al. 2005; SM20]. The SE based analysis presented below is conducted in a reference frame that moves with the low-level vortex. The cylindrical coordinate system (with radius r and azimuth φ) is centered on \mathbf{x}_l . The variables u, v and w respectively represent the radial, azimuthal and vertical velocity fields in the aforementioned coordinate system. As usual, an overbar (prime) is used to denote the azimuthal mean (perturbation) of a fluid variable.

550

552

553

554

556

557

559

560

563

566

SE theory assumes that the basic state of the vortex approximately maintains thermal wind balance during its evolution. The preceding assumption leads to a diagnostic equation for the streamfunction $\Psi(r,z)$ of the mean secondary circulation. This so-called *SE equation* is of the form $\mathcal{L}[\Psi] = \sum_{\alpha \in \{h,e,\mathcal{T}\}} F_{\alpha}$, in which \mathcal{L} is a linear differential operator and F_{α} is one of several source terms. For the present analysis, the source terms are formally attributable to applied heating (h), resolved eddy-forcing (e), and subgrid turbulent transport (\mathcal{T}) . Linearity of the SE equation allows the solution for Ψ to be written $\sum_{\alpha} \Psi_{\alpha}$, in which $\mathcal{L}[\Psi_{\alpha}] = F_{\alpha}$. Since the velocity field of the mean secondary circulation is obtained from a linear operation on Ψ , it too can be decomposed into the following sum of three parts:

$$\begin{pmatrix} \bar{u} \\ \bar{w} \end{pmatrix} \stackrel{\text{theory}}{=} \begin{pmatrix} \bar{u}_h \\ \bar{w}_h \end{pmatrix} + \begin{pmatrix} \bar{u}_e \\ \bar{w}_e \end{pmatrix} + \begin{pmatrix} \bar{u}_{\mathcal{T}} \\ \bar{w}_{\mathcal{T}} \end{pmatrix}. \tag{11}$$

Each component $(\bar{u}_{\alpha}, \bar{w}_{\alpha})$ on the right-hand side of Eq. (11) can be viewed as the secondary circulation that would be required to maintain thermal-wind balance under the imaginary situation in which only the forcing connected to F_{α} exists. The \mathcal{T} -component generally has separate contributions from turbulent momentum transport (friction) and turbulent heat transport, but the author has verified that the former dominates the latter in the lower troposphere for all of the illustrative cases considered below. Therefore, the \mathcal{T} -component is here viewed as being predominantly attributable to friction. The reader may consult appendix D for further details on the SE equation and its solution.

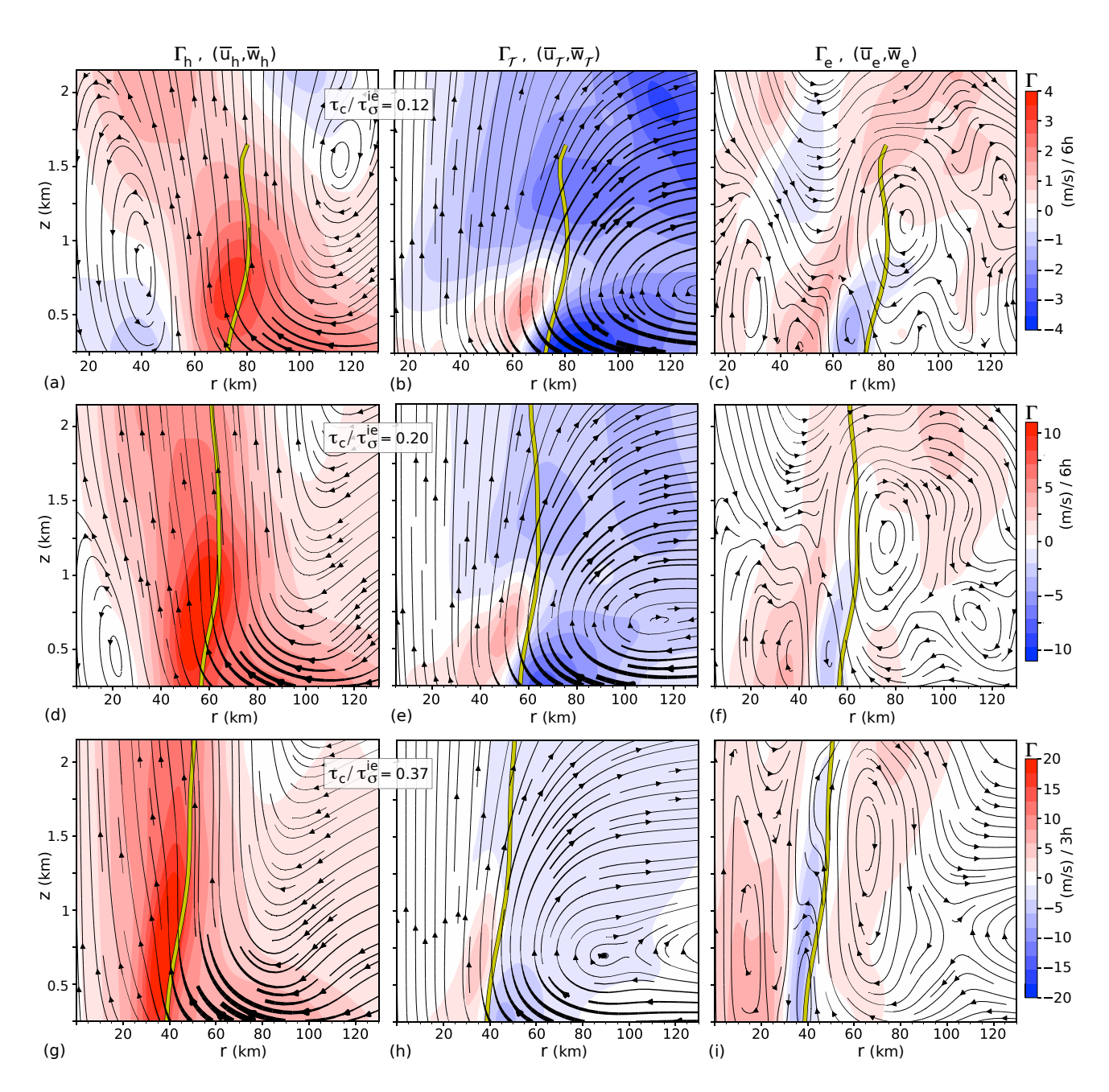


Fig. 12: SE-based analysis of intensification in several subcritical reference simulations. (a) Contributions to the mean secondary circulation (streamlines) and to $\partial \bar{v}/\partial t$ (color) formally attributable to down-tilt heating in the reference simulation with $a=4a_c/55$ and $\tau_c/\tau_\sigma^{ie}=0.12$, during an early 6-h interval of the IR measurement period. (b) As in (a) but for contributions primarily attributable to subgrid turbulent transport. (c) As in (a) but for contributions attributable to asymmetric eddy-forcing. Local streamline thickness is proportional to the local magnitude of the partial secondary velocity field, and is scaled uniformly in (a-c). The amber line traces the 6-h time average of the z-dependent radius of maximum \bar{v} in the lower troposphere. (d-f) As in (a-c) but for the reference simulation with $a=2a_c/11$ and $\tau_c/\tau_\sigma^{ie}=0.20$. (g-i) As in (a-c) but for a 3-h early interval of the IR measurement in the reference simulation with $a=4a_c/11$ and $\tau_c/\tau_\sigma^{ie}=0.37$.

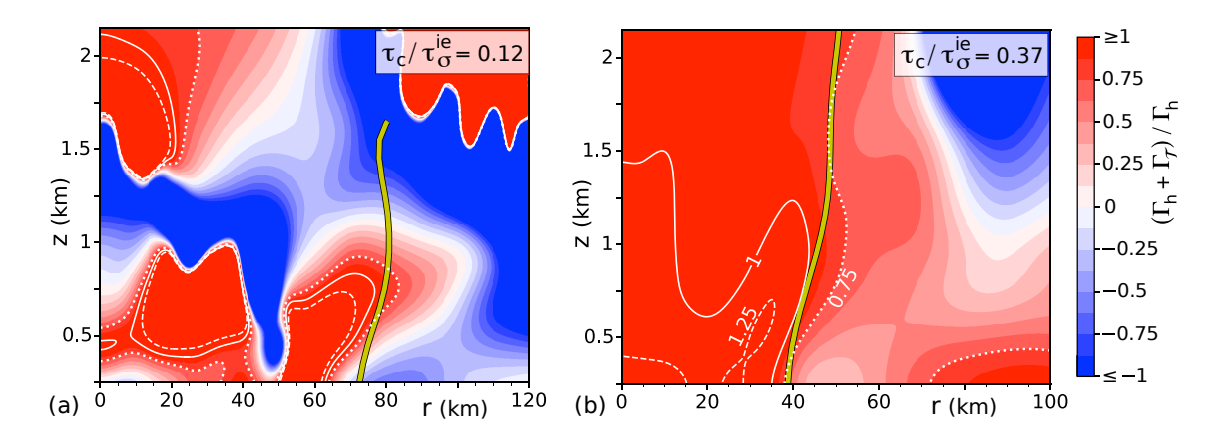


Fig. 13: (a) The ratio $\lambda \equiv (\Gamma_h + \Gamma_T)/\Gamma_h$ for the reference simulation with $\tau_c/\tau_\sigma^{ie} = 0.12$. The dotted, solid and dashed white lines respectively correspond to $\lambda = 0.75$, 1 and 1.25. The amber line traces the z-dependent radius of maximum $\bar{\nu}$, averaged over the time period of the SE analysis. (b) As in (a) but for the reference simulation with $\tau_c/\tau_\sigma^{ie} = 0.37$.

Let us now consider the following azimuthally averaged azimuthal velocity equation:

$$\frac{\partial \bar{v}}{\partial t} = -\bar{u}\bar{\eta} - \bar{w}\frac{\partial \bar{v}}{\partial z} + \bar{\mathcal{E}}_{v} + \bar{\mathcal{T}}_{v},\tag{12}$$

in which $\eta \equiv \zeta + f$, $\zeta \equiv \hat{\mathbf{z}} \cdot \nabla_H \times \mathbf{u}$, \mathcal{E}_v is resolved eddy-forcing (see appendix D) and \mathcal{T}_v accounts for parameterized subgrid turbulent transport. Substituting Eq. (11) into Eq. (12) yields

$$\frac{\partial \bar{v}}{\partial t} \stackrel{\text{theory}}{=} \Gamma_h + \Gamma_e + \Gamma_{\mathcal{T}},\tag{13}$$

573 in which

$$\Gamma_{h} \equiv -\bar{u}_{h}\bar{\eta} - \bar{w}_{h}\partial\bar{v}/\partial z,$$

$$\Gamma_{e} \equiv -\bar{u}_{e}\bar{\eta} - \bar{w}_{e}\partial\bar{v}/\partial z + \bar{\mathcal{E}}_{v},$$

$$\Gamma_{\mathcal{T}} \equiv -\bar{u}_{\mathcal{T}}\bar{\eta} - \bar{w}_{\mathcal{T}}\partial\bar{v}/\partial z + \bar{\mathcal{T}}_{v}.$$
(14)

Figure 12 shows the partial accelerations on the right-hand side of Eq. (13), and the secondary circulations regulating their advective terms, for several subcritical simulations belonging to the reference group. Each image focuses on the lower tropospheric dynamics within 130 km of the vortex center during an early stage of the intensification period. The acceleration associated with eddy forcing (Γ_e) tends to be negative in the vicinity of the strongest cyclonic winds near the surface, but is generally small compared to at least one of the other components of $\partial \bar{v}/\partial t$. When the diabatic forcing is weak such that $\tau_c/\tau_\sigma^{ie} = 0.12$, the usually (but not invariably) opposite accelerations associated with heating (Γ_h) and turbulent transport (Γ_T) alternate in having greater

magnitude as the altitude increases near the z-dependent radius of maximum \bar{v} (r_{zm}). As τ_c/τ_σ^{ie} grows to 0.37, the positive acceleration associated with heating becomes appreciably stronger than the action of turbulent transport.

Figure 13 more clearly demonstrates the rising dominance of diabatic forcing over frictional spindown by showing the ratio $\lambda \equiv (\Gamma_h + \Gamma_T)/\Gamma_h$. When λ is close to 1, Γ_h is dominant; otherwise Γ_T has comparable or greater magnitude. For the case of weakest diabatic forcing [Fig. 13a], λ generally falls well below unity— or is even negative —in the neighborhood of r_{zm} ; the only exception occurs in a thin vertical layer near z=0.75 km. For the case of strongest forcing [Fig. 13b], λ generally lies between 0.75 and 1 in the neighborhood of r_{zm} ; moreover, $|\lambda-1| \equiv |\Gamma_T/\Gamma_h| < 0.25$ over an extensive region of the inner core of the low-level vortex. $|\lambda-1| = |\Gamma_T/\Gamma_h| < 0.25$ over an extensive region of the inner core of the low-level vortex.

3d.4 Anticorrelation Between the Mean Convective Displacement and the Criticality Parameter

593

595

601

602

603

604

605

607

608

609

Earlier studies have suggested that faster spinup will result not only from stronger diabatic forcing, but also from decreasing the distance ℓ between the heat source and the low-level vortex center [cf. Pendergrass and Willoughby 2009; Vigh and Schubert 2009; S20]. It is therefore reasonable to wonder whether greater normalized IRs at higher values of the criticality parameter τ_c/τ_σ^{ie} might be partly attributable to smaller values of ℓ .

Figure 14a shows two distinct measurements of ℓ versus the criticality parameter. The inset shows ℓ at the start of the intensification period $(t = t_i)$, whereas the main graph shows the time average of ℓ over the entire intensification period $(t_i \le t \le t_e)$. First consider the subcritical simulations for which the base-10 logarithm of τ_c/τ_σ^{ie} (the abscissa of each graph) is appreciably negative. The inset reveals that for many simulation groups, there is virtually no variation of the initial value of ℓ among subcritical systems; therefore, the initial value of ℓ is not a robust indicator of normalized IR in the subcritical parameter regime. On the other hand, the main graph shows that in a given simulation group, the time average of ℓ tends to decay with growth of the criticality parameter. Such reduction of the time average of ℓ could conceivably contribute— alongside the diminishing relative influence of frictional damping —to the attendant growth of normalized IR.

 $^{^{10}}$ Bear in mind that because SE theory neglects unbalanced dynamics, Γ_h and Γ_T should not be expected to precisely match the accelerations induced by heating and frictional forcing imposed separately on a vortex. Nevertheless, one may provisionally assume that SE theory applied at weak-to-moderate tropical storm intensity offers a reasonable picture of the relative magnitudes of these two accelerations [SM20].

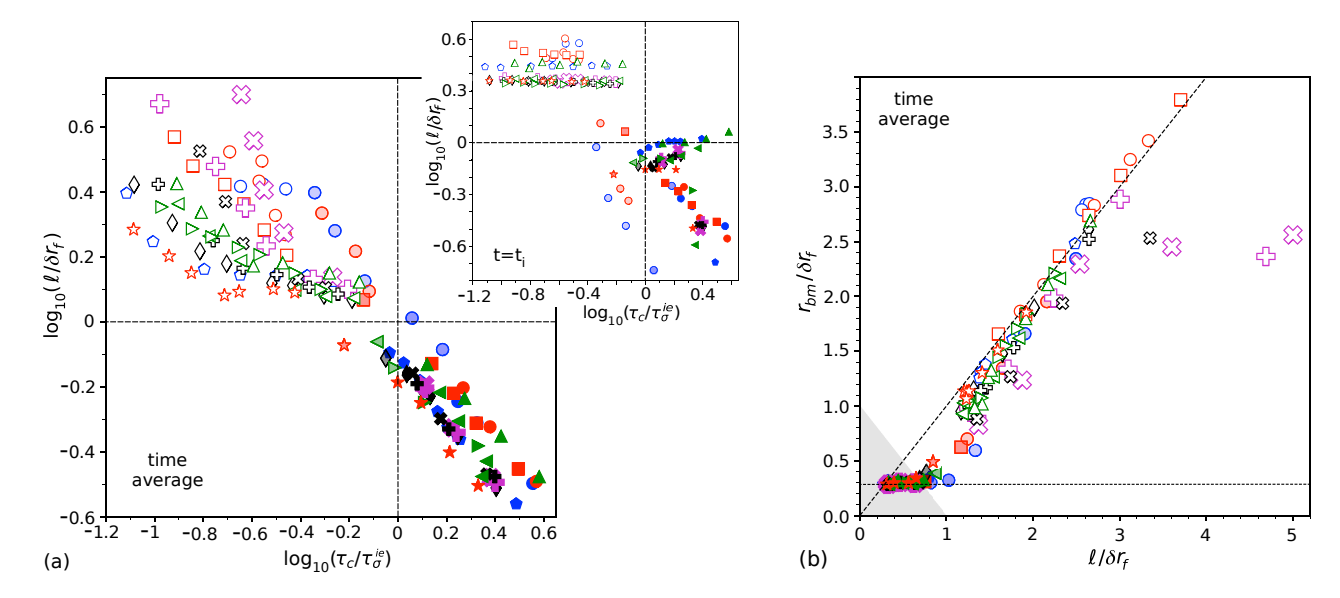


Fig. 14: (a) Main graph: base-10 logarithm of the mean value of ℓ during the IR measurement period versus the base-10 logarithm of the criticality parameter τ_c/τ_σ^{ie} . Inset: as in the main figure, but for ℓ at the start of the intensification period $(t=t_i)$. (b) The mean radius of maximum wind speed in the boundary layer versus the mean value of ℓ during the IR measurement period. The dashed slanted line corresponds to $r_{bm} = \ell$. The dotted horizontal line corresponds to the minimum accepted value for r_{bm} (10 km). The gray triangle is the region of parameter space where the nominal inner core of the low-level vortex lies entirely within the core of the heat source $(\ell + r_{bm} \le \delta r_f)$. Symbols are as in Fig. 11.

In the supercritical parameter regime, ℓ likewise decays as the criticality parameter grows, but the decay cannot be firmly linked to any major variation of normalized IR [Fig. 11]. Such insensitivity of the normalized IR may be connected to the following two facts: after core replacement, ℓ is generally smaller than the radial lengthscale δr_f of the diabatic forcing, and the measurement radius of v_{bm} (i.e., r_{bm}) usually reduces to the enforced 10-km minimum.

It is worth remarking that in contrast to the supercritical state of affairs, the time averages of ℓ and r_{bm} are positively correlated in subcritical systems for which core replacement never occurs (empty symbols) or unsuccessfully attempts to occur (light filled symbols) during the intensification period [Fig. 14b]. In fact, the two quantities generally become nearly equal as ℓ increases beyond approximately $2\delta r_f$.¹¹ It stands to reason that the decay of the time average of ℓ as τ_c/τ_σ^{ie} increases toward unity in a given simulation group generally goes hand in hand with a decay of the time average of r_{bm} .

¹¹The few anomalous cases in this parameter regime for which the time average of ℓ substantially exceeds that of r_{bm} correspond to sheared systems in which the diabatic forcing is too weak to prevent the gradual separation of the low-level and midlevel vortices.

3e. Low-level Vorticity Production

624

625

633

The transition from a slow intensification mechanism to a fast intensification mechanism initiated by core replacement in the 3D model is quantitatively consistent with shallow-water theory [S20] in occurring when the convergence generated by diabatic forcing exceeds τ_c^{-1} . This result was not a foregone conclusion, since unlike shallow-water dynamics, the horizontal contraction (vertical stretching) of a vortex-tube is joined by other vertical vorticity production mechanisms—
most notably vortex-tube tilting —within the convergence zone of a 3D system. Specifically, the vertical relative vorticity equation in the 3D model can be written as follows:

$$\frac{D\zeta}{Dt} = -\eta \nabla_{H} \cdot \mathbf{u} + \zeta_{H} \cdot \nabla_{H} w - c_{pd} \hat{\mathbf{z}} \cdot (\nabla_{H} \theta \times \nabla_{H} \Pi) + \hat{\mathbf{z}} \cdot (\nabla_{H} \times \mathbf{T}_{H}), \tag{15}$$

in which (as usual) D/Dt is the material derivative, ζ_H is the horizontal vorticity vector, $\Pi \equiv (p/p_r)^{R_d/c_{pd}}$ is the nondimensional Exner function of pressure p normalized to $p_r \equiv 10^5$ Pa, R_d (c_{pd}) is the gas constant (isobaric specific heat) of dry air, and \mathbf{T}_H is the horizontal velocity tendency associated with parameterized turbulence. The first term on the right-hand side of Eq. (15) essentially represents the effect of vortex-tube stretching, the second represents the effect of vortex-tube tilting, the third represents (positive or negative) baroclinic vorticity production, and the fourth represents vorticity production via subgrid turbulent transport.

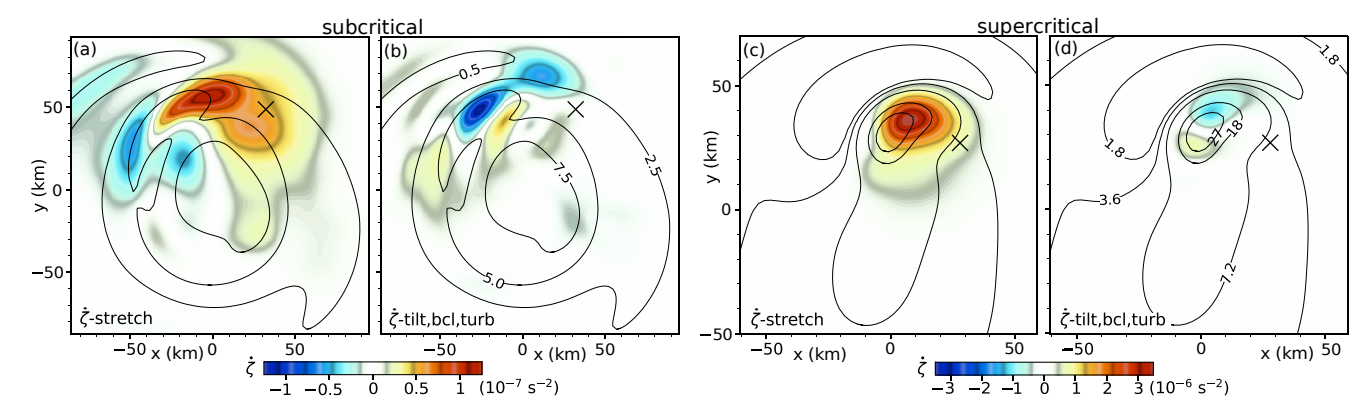


Fig. 15: (a) Vertical vorticity tendency $(\dot{\zeta})$ associated with vortex-tube stretching in the subcritical reference simulation with $\tau_c/\tau_\sigma^{ie}=0.20$ [Fig. 6], averaged over $4.0 \le t \le 5.5$ h and $z \le 3.1$ km. (b) As in (a) but for the vertical vorticity tendency attributable to vortex-tube tilting, baroclinicity, and parameterized subgrid turbulence combined. Black contours in (a) and (b) show the t-z average of ζ , labeled [in (b)] in units of 10^{-4} s⁻¹. The \times marks the time average of \mathbf{x}_f . The Cartesian (x,y) coordinate system is centered on the time average of \mathbf{x}_l . All fields are Gaussian-smoothed in x and y with a standard deviation parameter of 5 km. (c,d) As in (a,b) but for the supercritical reference simulation with $\tau_c/\tau_\sigma^{ie}=1.09$ [Fig. 8], and with the time averaging over $1 \le t \le 1.5$ h.

Figure 15 compares the stretching term to the sum of all other contributions to $D\zeta/Dt$ during the early developmental stages of typical subcritical and supercritical systems. The plotted tendencies are temporally averaged over relatively short time periods (see the caption) and vertically averaged from the surface to z = 3.1 km. The figure suggests that in the vicinity of down-tilt heating, the stretching term on the whole tends to be stronger than the sum of all other terms. The disparity is evidently more pronounced in the supercritical system, which happens to be in the midst of a core replacement event. The fairly dominant status of the stretching term helps explain why shallow-water theory is adequate for predicting the critical convergence required to initiate a core replacement event in the 3D model under present consideration.

4. Connection to Realistic Tropical Cyclone Dynamics

4a. Intensification Rates

641

642

643

645

646

648

649

651

652

At this point, one might appropriately ask how the preceding results relate to realistic tropical cyclone dynamics. The first issue is how the IRs compare to those in nature. A combination of theoretical reasoning and cloud resolving simulations led Wang and coauthors [2021 (WLX21)] to the following provisional formula for the maximum potential intensification rate (MPIR) of a tropical cyclone:

$$\frac{dv_{bm}}{dt} \stackrel{\text{MPIR}}{=} \frac{27}{256} \frac{\alpha C_d}{h_b} V_{max}^2, \tag{16}$$

potential intensity V_{max} . A preliminary analysis in WLX21 suggested that the preceding formula is reasonably consistent with observed MPIRs— for various environmentally determined values of V_{max} —extracted from 6-h intensification rates. Figure 16 shows the IRs of all intensifying vortices under present consideration, normalized to the MPIR of WLX21 with V_{max} set to a value (95 m s⁻¹) that is near the current upper-bound of observations [Kimberlain et al. 2016]. A sizeable subset of subcritical systems realistically have IRs below the MPIR. On the other hand, all supercritical cases exhibiting a well-established core replacement event have IRs more than three-times greater than the MPIR. This suggests that

in which $\alpha = 0.75$, $h_b = 2$ km and $C_d = 0.0024$ for sufficiently large values of the maximum

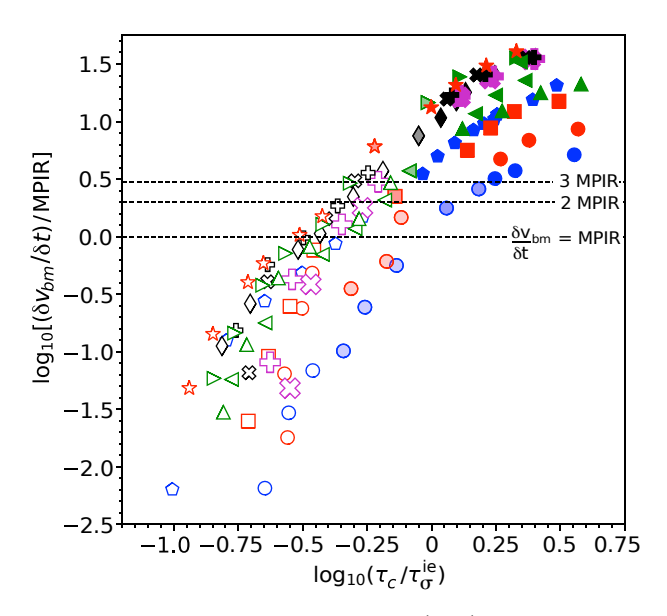


Fig. 16: IR of non-decaying vortices normalized to $3.08 \text{ m s}^{-1} \text{ h}^{-1}$, which equals the MPIR of WLX21 evaluated for tropical cyclones capable of achieving 95 m s⁻¹ maximum sustained wind speeds. Symbols are as in Fig. 11.

sustained intensification associated with core replacement *in our simulation set* would not be realistic. At best, the intensification following one of our simulated core replacement events could last only a brief period of time (no longer than a couple of hours) to permit a 6-h IR within natural bounds.¹² If the vortex were much weaker to begin with, or if the diabatic forcing happened to drift at a velocity closer to that of the local lower tropospheric background flow, so as to greatly increase τ_c , the supercriticality condition $\tau_c/\tau_\sigma > 1$ required for core replacement could be satisfied with a much larger value of τ_σ (much weaker heating). The associated IR, which scales as τ_σ^{-1} in the supercritical parameter regime, would be proportionally smaller and potentially realistic over a 6-h time period. Appendix E explains how the time scale for supercritical intensification might also lengthen upon introducing a secondary negative component to the down-tilt heat source.

4b. Diabatic Forcing

The diabatic forcing used for the present study was designed to roughly conform with observations and full-physics simulations of misaligned tropical cyclones in having deep cumulus convection concentrated down-tilt of the surface vortex center. Whether the morphological

¹²The model used for this study was not designed to remain realistic long after a core replacement event under general circumstances. Following such a dramatic structural transformation of the vortex in a real system, the diabatic forcing (moist convection) is expected to eventually reorganize, and diminish if abnormally intense.

details of the diabatic forcing are realistic merits further consideration. Data from the cloud 686 resolving simulations of S22 [specified in appendix F.a] provide a reasonable basis for comparison. 687 Figure 17 shows the nominal heating distributions of down-tilt convection in three tropical cy-688 clones from S22 with underlying sea-surface temperatures of 26 °C (left column), 28 °C (middle column) and 30 °C (right column). To be precise, each plot shows the azimuthal mean of the 690 material derivative of θ in a cylindrical coordinate system whose central axis passes through the 691 down-tilt heating center \mathbf{x}_f that is defined by Eq. (F1) of appendix F.b. The top plot in each 692 column corresponds to a time average over a selected 2-h analysis period when the system is at 693 depression or tropical storm intensity, whereas the bottom plot corresponds to an overlapping 6-h 694 average. Moderate differences of intensity and spatial structure between the "short" and "long" time averages of each heating distribution demonstrate that while down-tilt convection may be 696

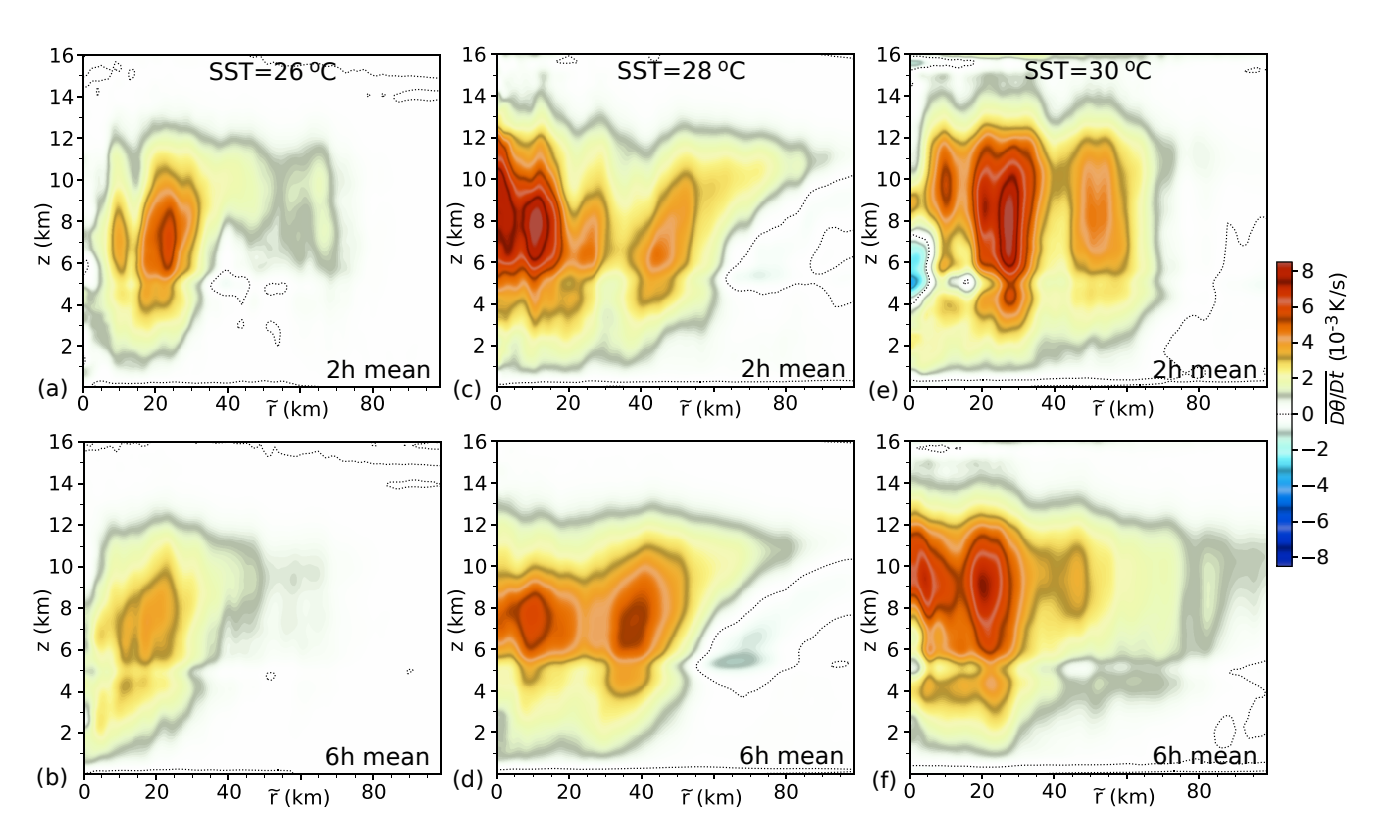


Fig. 17: Selected down-tilt heating profiles from the cloud resolving simulations of S22. (a) Two-hour and (b) overlapping 6-h time averages of the azimuthal mean of $D\theta/Dt$ about the central axis of down-tilt heating in a misaligned tropical cyclone over an ocean whose surface temperature is 26 °C [simulation T26-HRA (226 $\le t \le 232$ h) of Table F1]. (c,d) As in (a,b) but for a system with an SST of 28 °C [T28-HRA (160 $\le t \le 166$ h)]. (e,f) As in (a,b) but for a system with an SST of 30 °C [T30-HRA (61 $\le t \le 67$ h)].

persistent [appendix A of S20], the steady diabatic forcing employed for this study after ramping is inexact. Moreover, the S22 heating distributions suggest that in contrast to our simplified parameterization scheme [Eq. (1)], the peak of the diabatic forcing is not constrained to lie on its central axis. In further contrast, the S22 heating distributions often have appreciable azimuthal variation around their central axes (not shown).

Figure 18 provides a more elaborate and quantitative analysis of the S22 data set. Figure 18a shows the distance ℓ between the heating center and the low-level vortex center versus the tilt magnitude. Here and in all other subplots, each data point with error bars corresponds to a 6-h interval during the pre-hurricane evolution of a tropical cyclone. The 6-h interval is divided into three 2-h segments. The coordinates of each data point (marked by a solid symbol) correspond to the medians of the 2-h time-averages of the plotted variables. The error bars extend from the minimum 2-h time average to the maximum. The condition that ℓ remain comparable to the tilt magnitude (enforced herein except in RFOUT) appears to be reasonably consistent with the unconstrained results of S22. Figure 18b shows that the angle φ_f of the position vector of the heating center (in a coordinate system centered at \mathbf{x}_ℓ) measured counterclockwise from the direction of the tilt vector is generally negative, but reasonably close to zero as assumed for the reference group and most other simulations examined for the present study. Only a few exceptional cases coinciding with relatively small values of ℓ have magnitudes of φ_f exceeding 45^o .

Figures 18c-f contain information on the intensity and lengthscales of the heating distribution. All but one of the plotted parameters are obtained from a nonlinear least-squares fit of the 2-h heating distribution [exemplified in the top row of Fig. 17] to a function equivalent to the right-hand side of Eq. (1), but with $T \to 1$ and $\tilde{r} \to \tilde{r} - d_f$ so as to permit a radial offset d_f of the heating maximum. The parameter unrelated to the fit-function is Q, which corresponds to the vertical integral of the heating rate density ($\rho_d q$ defined in appendix F.b) between 1 and 16 km above sea-level, averaged within a 100-km radius of the heating center. Figure 18c shows the peak value of the heating distribution given by the fit function (a) along with the coinciding values of Q. The values of a are within the range used—mostly for subcritical systems—in the present study. The same can be said for the values of Q, which for the reference group equals 4.9 kW m⁻² × ($a/10^{-2}$ K s⁻¹). While the average (positive or negative) error bar plotted for Q is merely 0.2 times the median of Q for a

¹³Repetition of the fit with d_f constrained to equal 0 gives a similar range of results for a.

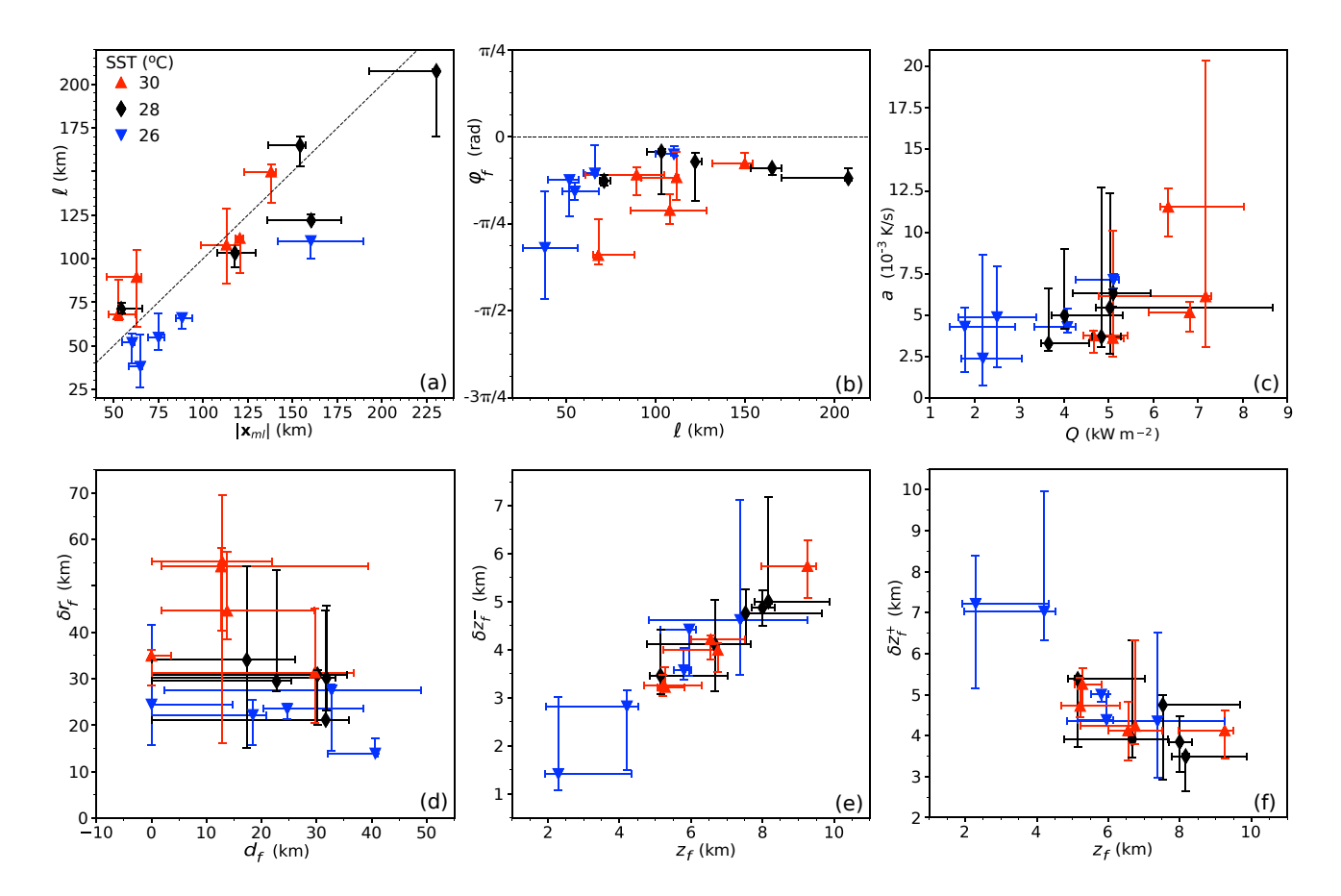


Fig. 18: Characteristics of down-tilt heating for a number of tropical depressions and tropical storms in the S22 data set. (a) Relationship between the tilt magnitude $|\mathbf{x}_{ml}|$ and the horizontal distance ℓ from the heating center to the low-level vortex center. The slanted dashed line corresponds to $\ell = |\mathbf{x}_{ml}|$. Different symbol shapes and colors correspond to simulations with different SSTs as shown in the legend. (b) Azimuthal displacement φ_f of the heating center from the direction of the tilt vector, plotted against ℓ . (c) Strength parameter a of the fit-function for the down-tilt heating distribution plotted against the vertically integrated down-tilt heating density Q. (d) The radial shape parameters for the down-tilt heating distribution. (e) The downward decay length δz_f^- of the down-tilt heating distribution plotted against the height of maximum heating in the fit-function. (f) As in (e) but with the upward decay length δz_f^+ replacing δz_f^- .

given 6-h interval, the average error bar plotted for a is 0.6 times its median. It stands to reason that two-hourly variations of details in the structure of the diabatic forcing are more substantial than such variations of the net heating rate. Substantial structural variation is corroborated by the graph of the radial shape parameters of the fit function [Fig. 18d]. Note however, that the constant radial shape parameters chosen for the diabatic forcing in this study ($d_f = 0$, $\delta r_f = 35$ km) are within the depicted range of possibilities. The vertical shape parameters [Figs. 18e-f] are somewhat more stable over given 6-h periods. Furthermore, the triplet (z_f , δz_f^- , δz_f^+) = (7.5, 6.0, 3.5) km prescribed for most of the simulations herein seems to fall within the spread of the S22 data set.

The preceding considerations offer some reassurance that the form of the diabatic forcing used for the present study is not egregiously detached from reality, or at least from what might be found in a cloud resolving model. The use of a steady heating distribution may leave a somewhat incomplete picture of the dynamics, but the complications associated with moderate temporal fluctuations can be readily examined in the future [cf. S20]. There may also be circumstances worthy of future study in which a purely positive heat source inadequately represents down-tilt convection [cf. appendix E]. In considering the potential shortcomings of the diabatic forcing, one should further bear in mind that the heating rate applied at any point in the vortex is dynamically independent of the history and instantaneous vertical velocity of the local air parcel. In principle, this could introduce some slightly unrealistic features of 3D convection in our model. That being said, analysis of several reference simulations (not shown) has suggested that a qualitatively realistic statistical correlation tends to develop between $\dot{\theta}_f$ and w at lower and middle tropospheric levels above the near-surface layer.

5. Conclusions

The study at hand aimed to gather insights into the mechanisms by which a misaligned tropical cyclone may intensify when deep convection is concentrated down-tilt of the surface-vortex center. The methodology involved conducting numerous simulations with a 3D nonhydrostatic model that incorporates an imposed heat source to generate down-tilt convection. The simulations were divided into over a dozen groups that differed from one another in the initial vortex strength, the initial tilt magnitude, the environmental shear flow, the prescribed displacement of down-tilt heating from the moving midlevel vortex center, or the vertical heating profile. Variation of vortex intensification in each simulation group was controlled by adjusting the magnitude of the heat source. The following key results were obtained:

• Distinct modes of intensification occur depending on whether the boundary layer convergence τ_{σ}^{-1} in the vicinity of the down-tilt heat source is above or below a critical value. The critical value τ_{c}^{-1} found in each simulation group agrees with shallow-water theory [S20] in approximately equaling two-times the magnitude of the vector difference between the drift velocity of the heating

center and the local velocity of the nondivergent background flow, divided by the radial lengthscale of the heat source [see Eq. (9)]. If the convergence is supercritical, such that τ_c/τ_σ exceeds unity, boundary layer fluid entering the convergence zone becomes horizontally trapped, and its vertical vorticity continuously amplifies. The result is the local emergence of a small-but-strong vorticity core that eventually dominates the parent cyclone and rapidly intensifies. If the system is subcriti-cal, boundary layer fluid generally passes through the convergence zone, where it experiences only a transient episode of vorticity enhancement while losing some of its original mass to vertical convection. The fluid with moderately enhanced vorticity typically recirculates around the inner core of the broader cyclone. Meanwhile, if the diabatic forcing is not too weak, the inner core progressively contracts and slowly intensifies. Bear in mind that some deviation from the preceding scenario can occur at relatively large subcritical values of τ_c/τ_σ [see sections 3c and 3d.2].

- Quantitatively, the fast mode of supercritical intensification that follows core replacement occurs at a rate that is measured to be approximately proportional to v_i/τ_σ , in which v_i [precisely defined in section 3d.2] is a characteristic velocity scale that increases with the initial mean absolute vorticity in the broader vicinity of the heat source. In other words, the normalized intensification rate (IR) defined by $(\delta v_{bm}/\delta t)\tau_\sigma/v_i$ is roughly constant. In the subcritical parameter regime, the normalized IR was found to decline approximately linearly with decreasing values of τ_c/τ_σ to the point of becoming negative owing to the emergent dominance of frictional spindown. A limited number of simulations with negligible surface drag have suggested [in agreement with S20] that even without frictional dissipation, the time scale of subcritical intensification normalized to τ_σ can exhibit multifold growth as the diabatic forcing tends toward zero [Fig. 4].
- In all of the simulation groups, the strength of diabatic forcing required to induce a supercritical down-tilt core replacement event would cause unrealistically fast intensification when viewed over a typical observational time scale of 6 h or longer. It stands to reason that such strong forcing would have to end shortly after core replacement in a natural tropical cyclone. In principle, supercritical conditions are possible with weaker diabatic forcing that could realistically last well beyond core replacement. Compared to the systems considered herein, the drift velocity of the down-tilt convection zone would most likely have to be closer to the local velocity of the lower

tropospheric background flow, so as to substantially increase τ_c [see also appendix E].

While this study has clearly illustrated some basic differences between subcritical and supercritical modes of asymmetric intensification, there is undoubtedly more to learn, especially on the subject of subcritical intensification. In the linear model used to describe the subcritical relationship between the normalized IR and τ_c/τ_σ , the slopes and points of zero IR obtained from the simulation groups showed some spread that is yet to be fully elucidated. One might reasonably expect to find far greater variability in nature, owing to greater diversity in the structure and propagation dynamics of down-tilt convection. In theory, such diversity could even add branches to the normalized IR curve associated with distinct pathways of low-level spinup [cf. S20]. Let it suffice to say for now that further research will be needed to obtain a truly comprehensive understanding of subcritical dynamics.

Acknowledgments: The author thanks three anonymous reviewers for their constructive feedback and suggestions on how to improve several aspects of this article. The author also thanks Dr. George Bryan of the National Center for Atmospheric Research (NCAR) for providing the original atmospheric model (CM1) that was tailored for this study to simulate the intensification of tropical cyclone-like vortices subjected to down-tilt diabatic forcing. This study was supported by the National Science Foundation under Grants AGS-1743854 and AGS-2208205. A number of simulations conducted for this study were made possible with resources provided by NCAR's Computational and Information Systems Laboratory (doi:10.5065/D6RX99HX).

Data Availability Statement: CM1 code modifications and input files for selected simulations, which together may be used to help reproduce the main results of this study, will be available at doi:10.5281/zenodo.7637579 upon publication of this paper. Archived simulation output files are presently available to researchers upon request sent to schecter@nwra.com.

Appendix A: Vortex and Convergence Centers

Let \mathbf{x}_{δ} represent the horizontal position vector of the vortex center in a vertical layer indicated by the subscript δ . In general, \mathbf{x}_{δ} corresponds to the location at which one must place the origin of a polar coordinate system to maximize the peak value of $\bar{v}_{\delta}(r)$ for $r \geq r_c$, in which \bar{v}_{δ} is the vertical average of the azimuthal-mean tangential velocity in layer- δ , and r_c is a specified minimal core radius. For the analysis of simulation data presented throughout the main text, \mathbf{x}_l is the vortex center in a 1.2-km thick boundary layer adjacent to the sea-surface, whereas \mathbf{x}_m is the vortex center in the middle tropospheric layer defined by 7.1 < z < 8.5 km. In both cases, $r_c = 10$ km. By contrast, \mathbf{x}_{l2} is the vortex center in the 1.2-km thick boundary layer obtained with $r_c = 70$ km.

Slightly different definitions are used for \mathbf{x}_l and \mathbf{x}_m to calculate the right-hand side of the equation for $d\mathbf{x}_f/dt$ in the parameterization of diabatic forcing that is added to CM1. The redefinitions are intended partly to improve computational efficiency, and partly to reduce large short-lived fluctuations of the heating center that may occur in conjunction with similar fluctuations of the tilt vector. Specifically, the layer corresponding to \mathbf{x}_l (\mathbf{x}_m) is collapsed onto the horizontal plane at z = 1.2 (7.8) km— so that no vertical averaging is necessary for the computation of \bar{v}_δ —and r_c is set to 55 km. The search for $\mathbf{x}_\delta(t)$ is also limited to a 300×300 km² region centered on $\mathbf{x}_\delta(t-\Delta t)$, in which Δt is the time-step of the simulation.

Figure A1 illustrates how the tilt vector $\mathbf{x}_{ml} \equiv \mathbf{x}_m - \mathbf{x}_l$ used for the runtime parameterization of diabatic forcing in a simulation can deviate from that which would result from replacing the vortex centers with those used for the post-runtime data analysis in the main text. Notable differences tend to emerge when the radius of maximum wind speed of the low-level or midlevel vortex decreases below the 55-km cut-off value in the runtime search algorithm. Differences will of course diminish when the small-scale and medium-scale circulations become increasingly concentric in each layer. Finally, the main text contains several references to the convergence center \mathbf{x}_{σ} of the boundary layer velocity field. In analogy to the vortex center, the convergence center is defined to be the origin of the polar coordinate system that maximizes the peak value of $-\bar{u}_b(r)$ for $r \ge r_c$, in which \bar{u}_b is the azimuthally averaged radial component of \mathbf{u}_b . The value of r_c is set to the minimum horizontal grid spacing of 2.5 km, but in contrast to the vortex center finding algorithm, an effective 20-km smoothing operation is applied to the velocity field before the search for \mathbf{x}_{σ} begins.

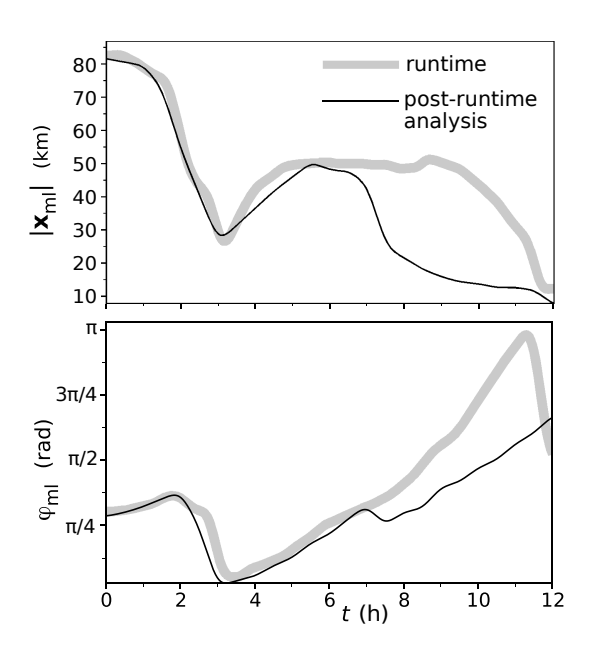


Fig. A1: Top: comparison of the magnitudes of the tilt vectors computed with the vortex centers that are used for (gray) the runtime parameterization of diabatic forcing and (black) post-runtime data analysis in the reference simulation with $\tau_c/\tau_\sigma^{ie} = 0.37$ [Fig. 7]. Bottom: similar comparison of the runtime tilt angle (φ_{ml}) and post-runtime tilt angle measured counterclockwise from the positive-x direction in Fig. 7.

Appendix B: Sensitivity to C_d

Section 3a [Fig. 4] addresses the consequences of eliminating surface drag on the time scale of vortex intensification, but does not thoroughly examine C_d -sensitivity. Figure B1 offers a more comprehensive picture of how the normalized IR varies as C_d increases from zero toward the upper extreme of inferred oceanic values [see Bell et al. 2012]. The plotted data primarily come from six groups of simulations configured with constant C_d : two groups with zero or near-zero surface drag (CD0 and CD0+), and four groups labeled CDX with $C_d = 0.00 \times 1.4$ Apart from modification of the surface drag coefficient at t = 0, all of the preceding simulation groups are set up like the reference group. Data from the reference group, for which $0.001 \le C_d \le 0.0024$, are shown for context. Note that the values of v_i (τ_c) for all plotted simulations have a standard deviation of only 7% (10%) of the mean. It stands to reason that v_i and τ_c can be viewed approximately as constants in the axis labels.

¹⁴Thus, $C_d = 0.005$ for group CD5, $C_d = 0.003$ for group CD3, $C_d = 0.001$ for group CD1, and $C_d = 0.0005$ for group CD05.

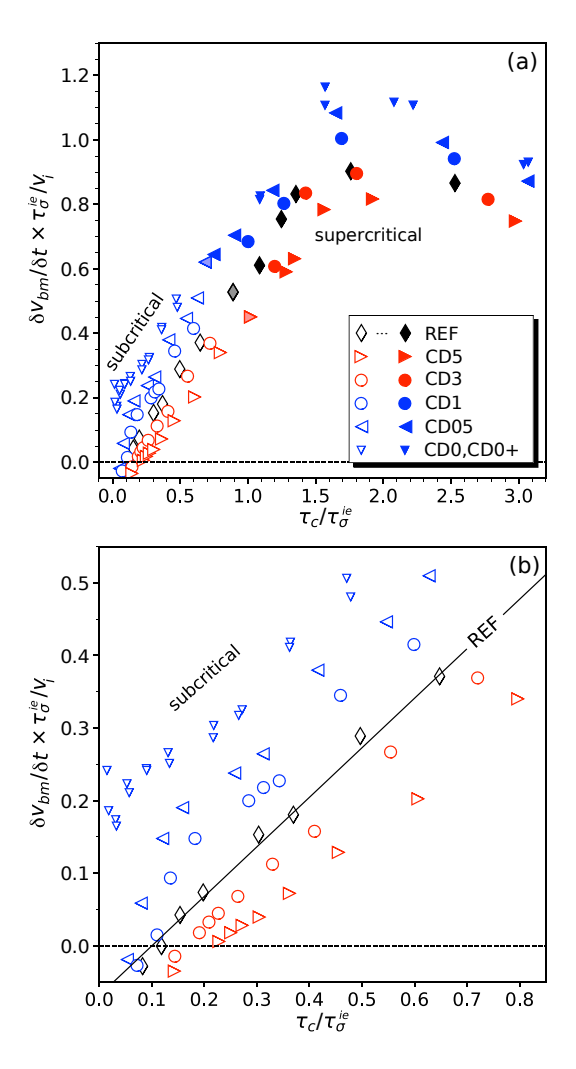


Fig. B1: (a) Nondimensional IR plotted against the criticality parameter for a number of simulation groups with different surface drag parameterizations. Symbol shading is as in Fig. 11. (b) Enlargement of the subcritical section of (a). The solid diagonal line is a linear regression for the reference group (REF).

Figure B1 shows that increasing C_d generally decreases the normalized IR at a fixed value of the criticality parameter τ_c/τ_σ^{ie} , and increases the threshold of τ_c/τ_σ^{ie} that is required for diabatic forcing to overcome frictional damping. As in the reference group, the subcritical growth of normalized IR with the criticality parameter is roughly linear for the two simulation groups with larger drag coefficients (CD3 and CD5). By contrast, the slope of the IR curve appears to markedly steepen as the criticality parameter decreases toward the point of zero IR in the two simulation groups with relatively small but finite drag coefficients (CD1 and CD05). Understanding the details of this nonlinearity is deferred to future study. The simulations with zero surface drag are exceptional in that the normalized IR appears to settle on a finite positive value as the convergence

time scale tends toward infinity and the criticality parameter approaches zero. As a final remark, the variation of surface drag considered herein does not appear to have a major effect on the transition zone (at $\tau_{\sigma}^{ie} \approx \tau_c$) separating systems that undergo core replacement (dark-filled symbols) from those that do not (white-filled symbols).

Appendix C: Group-Statistics for v_i and τ_c

878

879

881

882

883

884

885

886

888

Table C1 firstly summarizes the statistics of the scaling velocity v_i that appears in the expression for the normalized intensification rate of Fig. 11. The means and standard deviations are shown for both subcritical (column $v_{i,sub}$) and supercritical (column $v_{i,sup}$) systems in each simulation group. The fractional deviations from the mean are usually small within either parameter regime of a particular simulation group, suggesting that the subcritical and supercritical values of v_i can be viewed as approximate constants. Differences between subcritical and supercritical means are noticeable but generally minor. On the other hand, the mean value of v_i in either parameter regime can change appreciably from one simulation group to another. Such can be seen by comparing values from (for example) the groups labeled REF and WEAKV-TLTX3.

Group Name	$v_{i,\text{sub}}$ (m/s)	$v_{i,\text{sup}}$ (m/s)	τ_{c} (h)
REF	14.22 ± 0.50	15.53 ± 0.40	0.30 ± 0.02
TLTX2	7.65 ± 1.09	8.61 ± 0.20	0.36 ± 0.06
TLTX3	6.97 ± 2.44	4.70 ± 0.03	0.38 ± 0.06
SH2P5	13.95 ± 0.00	15.18 ± 0.60	0.29 ± 0.03
SH2P5⊥	14.03 ± 0.03	15.39 ± 0.55	0.27 ± 0.02
SH5	13.97 ± 0.11	15.19 ± 0.52	0.27 ± 0.02
SH5⊥	14.00 ± 0.00	15.66 ± 0.48	0.24 ± 0.03
RFOUT	9.25 ± 0.43	12.53 ± 0.46	0.34 ± 0.07
PHIFM45	14.04 ± 0.55	15.11 ± 0.35	0.34 ± 0.05
PHIFP45	14.45 ± 0.06	15.81 ± 0.45	0.25 ± 0.02
ZFUP	14.44 ± 1.00	16.64 ± 0.24	0.29 ± 0.02
WEAKV	8.69 ± 0.06	10.15 ± 0.15	0.44 ± 0.04
WEAKV-TLTX3	4.45 ± 0.88	3.68 ± 0.05	0.56 ± 0.10

TABLE C1. Left and middle data columns: scaling velocities for subcritical (sub) and supercritical (sup) systems, each expressed as a group mean \pm one standard deviation rounded to two decimal places. Right data column: time scale for background advection across the heat source.

Table C1 also summarizes the group-statistics of the time scale τ_c for background advection across the down-tilt heat source measured during the early phase of intensification, as explained in section 3d.2. Although the mean of τ_c can change appreciably from one simulation group to another (compare values associated with SH5 \perp and WEAKV-TLTX3), the standard deviation for a given group is usually small. The small standard deviation implies that variation of τ_c/τ_σ^{ie} (the abscissa in Fig. 11) within any particular group mainly results from variation of τ_c^{ie} .

Appendix D: Sawyer-Eliassen Computations

The following briefly summarizes the SE equations for each component Ψ_{α} of the streamfunction of the azimuthally averaged secondary circulation, and several approximations that are used to solve them. The reader may consult appendix D of SM20 for a more thorough discussion. The only notable difference between the SE analysis of this paper and that of SM20 is the substitution of applied diabatic forcing for the cloud-microphysical heat source.

As mentioned in the main text, the SE equation for each streamfunction is of the form

$$\mathcal{L}[\Psi_{\alpha}] = F_{\alpha},\tag{D1}$$

in which \mathcal{L} is a linear differential operator. Specifically,

$$\mathcal{L}[\Psi_{\alpha}] \equiv \partial_{z} \left(\frac{I \partial_{z} \Psi_{\alpha} + B \partial_{r} \Psi_{\alpha}}{\bar{\rho} r} \right) + \partial_{r} \left(\frac{S \partial_{r} \Psi_{\alpha} + B \partial_{z} \Psi_{\alpha}}{\bar{\rho} r} \right), \tag{D2}$$

in which the baroclinicity, static stability, and modified inertial stability parameters are respectively given by

$$B \equiv -\partial_z(C\bar{\kappa}),$$

$$S \equiv -g\partial_z\bar{\kappa}, \text{ and}$$

$$I \equiv \bar{\kappa}\bar{\eta}\bar{\xi} + BC/g.$$
(D3)

In addition, the forcing functions for $\alpha \in \{h, e, \mathcal{T}\}$ satisfy

917

918

934

$$F_{h} \equiv \partial_{z} \left(C \overline{\kappa^{2} \dot{\theta}_{f}} \right) + g \partial_{r} \left(\overline{\kappa^{2} \dot{\theta}_{f}} \right),$$

$$F_{e} \equiv -\partial_{z} \left(C \bar{\mathcal{E}}_{\kappa} \right) - g \partial_{r} \bar{\mathcal{E}}_{\kappa} - \partial_{z} \left(\bar{\kappa} \bar{\xi} \bar{\mathcal{E}}_{v} \right), \text{ and}$$

$$F_{\mathcal{T}} \equiv \partial_{z} \left(C \overline{\kappa^{2} \mathcal{T}_{\theta}} \right) + g \partial_{r} \left(\overline{\kappa^{2} \mathcal{T}_{\theta}} \right) - \partial_{z} \left(\bar{\kappa} \bar{\xi} \bar{\mathcal{T}}_{v} \right).$$
(D4)

In the preceding equations, $C \equiv \bar{v}^2/r + f\bar{v}$, $\bar{\eta} \equiv \bar{\zeta} + f$, $\bar{\xi} \equiv 2\bar{v}/r + f$, $\kappa \equiv \theta^{-1}$, ρ is mass density, and g is the gravitational acceleration near the surface of the earth. The variable \mathcal{T}_{θ} (\mathcal{T}_{v}) represents forcing by parameterized subgrid turbulence in the potential temperature (tangential velocity) equation. The variables associated with resolved "eddies" are given by

The last term on the right-hand side of the $\bar{\mathcal{E}}_{v}$ equation (having c_{pd} as a coefficient) is generally

$$\bar{\mathcal{E}}_{v} \equiv -\overline{u'\zeta'} - \overline{w'\partial_{z}v'} - c_{pd}\overline{\theta'\partial_{\varphi}\Pi'}/r, \text{ and}$$

$$\bar{\mathcal{E}}_{\kappa} \equiv -\overline{u'\partial_{r}\kappa'} - \overline{v'\partial_{\varphi}\kappa'}/r - \overline{w'\partial_{z}\kappa'}.$$
(D5)

subdominant. As usual, the symbol ∂_x appearing in various expressions above is shorthand for 919 $\partial/\partial x$, in which x is a generic variable. For all computations of Ψ_{α} , ellipticity of the SE equation is restored where violated below 921 z = 400 m by adjusting the static stability as described in SM20, with the adjustment parameter (nu) 922 given by 0.001. The solution to the SE equation is then obtained by a straightforward numerical 923 method that enforces the boundary condition $\Psi_{\alpha} = 0$ at r = 0, r = 898 km, z = 0 and z = 29.2 km. 924 Once the SE equation is solved, the component of the azimuthally averaged secondary circulation 925 associated with Ψ_{α} can be calculated from the following formula: $(\bar{u}_{\alpha}, \bar{w}_{\alpha}) = (-\partial_z \Psi_{\alpha}, \partial_r \Psi_{\alpha})/(r\bar{\rho})$. 926 Using a method of approximation similar to that of SM20, all azimuthally averaged variables appearing in the coefficients and forcing terms of the SE equation for Ψ_{α} are time averaged over 928 the moderately short analysis period. Similar time averages are used for $\bar{\eta}$, $\partial \bar{v}/\partial z$, $\bar{\mathcal{E}}_{v}$ and $\bar{\mathcal{T}}_{v}$ in the 929 expressions for Γ_{α} that are provided in the main text [Eq. (14)]. The time averages are obtained from data sampled every 90 s over the interval $2.5 \le t \le 5.5$ h for the subcritical system with 931 $\tau_c/\tau_\sigma^{ie}=0.37$, every 180 s over the interval $4 \le t \le 10$ h for the subcritical system with $\tau_c/\tau_\sigma^{ie}=0.20$, 932 and every 180 s over the interval $6 \le t \le 12$ h for the subcritical system with $\tau_c/\tau_\sigma^{ie} = 0.12$.

Appendix E: Hypothetical Effect of a Dipolar Component to Down-Tilt Heating on the Critical Convergence Required for Core Replacement

As noted in the main text, S20 theorized that a point of attraction would exist and core replacement would occur in the region of down-tilt convergence provided that $\tau_c/\tau_\sigma > 1$, or equivalently that $\sigma_{bf} > \tau_c^{-1}$. This condition [with τ_c essentially given by Eq. (9)] was derived under the assumption that the (low-level) down-tilt flow structure can be approximated by a solitary convergence zone embedded in a larger scale background flow. Such an assumption is a reasonable approximation for the simulations conducted herein, which represent down-tilt convection with a purely positive Gaussian-like heat source, and also has relevance to a certain class of "realistically" simulated tropical cyclones [see appendix A of S20]. On the other hand, one might imagine a scenario in which a neighboring downdraft associated with evaporative cooling creates a substantial low-level divergence zone in close proximity to the down-tilt convergence zone that persists over a time scale relevant to core replacement. It is of interest to consider how this might affect the critical convergence above which core replacement should occur.

For simplicity, suppose that the initial boundary layer velocity field in the neighborhood of downtilt convection, and in a reference frame moving with the convection, can be approximated by

$$\tilde{\mathbf{u}}_b = V_l \hat{\mathbf{y}} - \frac{\sigma_+ \delta r_+}{2} \frac{\min(\delta r_+, r_+)}{\max(\delta r_+, r_+)} \hat{\mathbf{r}}_+ + \frac{\sigma_- \delta r_-}{2} \frac{\min(\delta r_-, r_-)}{\max(\delta r_-, r_-)} \hat{\mathbf{r}}_-. \tag{E1}$$

Here, $V_l\hat{\mathbf{y}}$ is a spatially uniform velocity field representing the large-scale background flow. The middle (far-right) term accounts for a relatively small, circular convergence (divergence) zone. The variables σ_+ , δr_+ and r_+ (σ_- , δr_- and r_-) respectively denote the strength, radial width and distance from the center of the convergence (divergence) zone. The variable $\hat{\mathbf{r}}_+$ ($\hat{\mathbf{r}}_-$) is the radial unit vector of a polar coordinate system whose origin is at the center of the convergence (divergence) zone.

In the preceding notation, the critical convergence above which a point of attraction exists *in the*

absence of a divergence zone is given by $\tau_c^{-1} = 2V_l/\delta r_+$ [S20]. Figures E1a and E1b depict the streamlines of $\tilde{\mathbf{u}}_b$ for a system having a firmly subcritical solitary convergence zone characterized by $\sigma_+ = 1.25V_l/\delta r_+$ and $\sigma_- = 0$. The depiction suggests that a fluid volume entering the convergence zone will pass through, after losing some of its mass to vertical convection. Figures E1c and E1d illustrate how the local flow structure changes when a moderately weaker divergence zone with

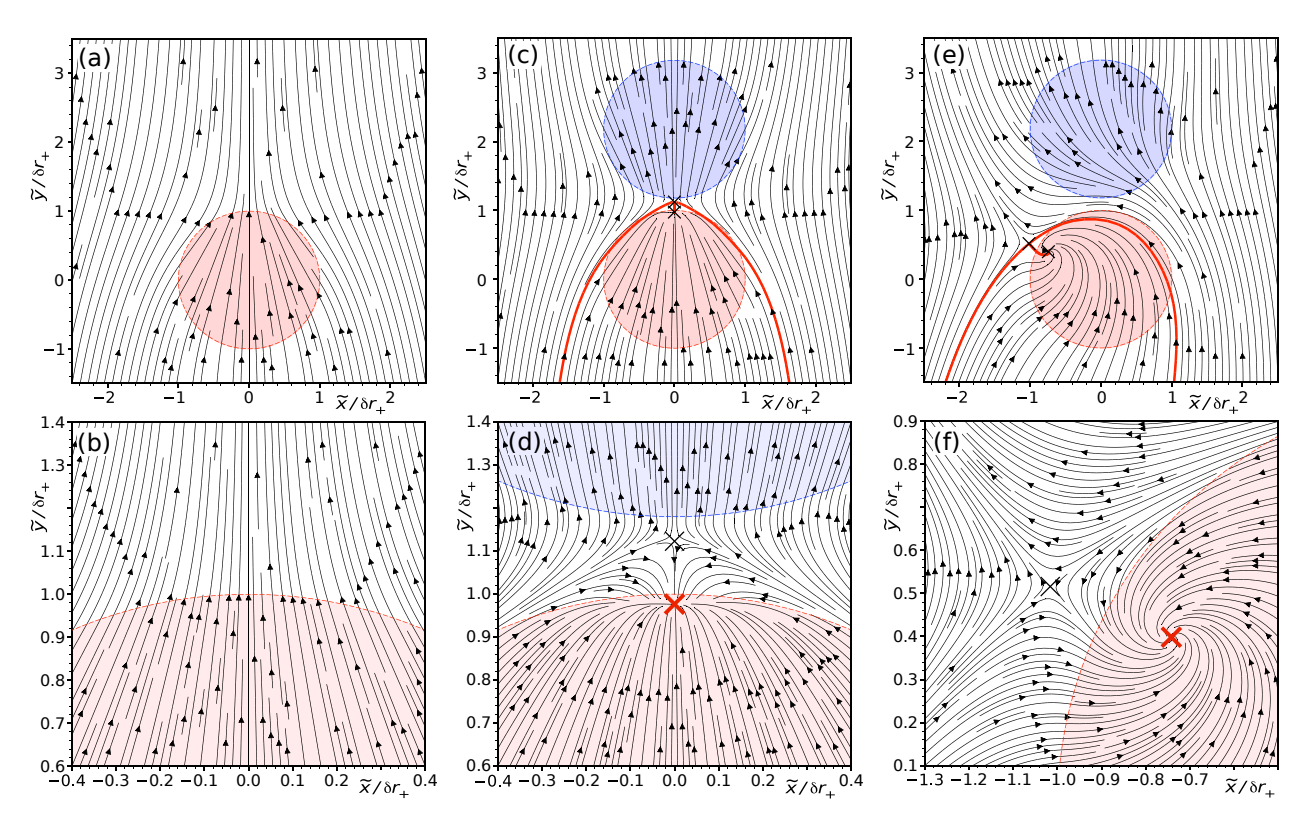


Fig. E1: (a) Streamlines in the vicinity of a subcritical solitary convergence zone (red circle) embedded in a large-scale background flow. The Cartesian coordinates \tilde{x} and \tilde{y} are measured from the center of the convergence zone. (b) Enlargement of (a) near the downwind edge of the convergence zone. (c,d) As in (a,b), but with the addition of a moderately weaker divergence zone (blue circle). The ×s mark stagnation points; the thick red × in (d) is the nominal point of attraction. The thick red curve in (c) corresponds to a streamline very close to the separatrix. (e,f) As in (c,d) but with positive/negative vorticity anomalies added to the convergence/divergence zone.

 $\sigma_- = 0.75\sigma_+$ and $\delta r_- = \delta r_+$ is placed at a distance of $2.18\delta r_+$ from the center of the convergence zone, directly downwind with respect to the background flow. The modification has introduced a point of attraction near the downwind edge of the convergence zone, which could in principle enable a core replacement event. The region below the red curve in Fig. E1c provides an initial estimate of the fluid destined to become horizontally trapped in the convergence zone, where its vorticity may continuously amplify. Figures E1e and E1f illustrate what would happen to the streamlines if the convergence and divergence zones were given uniform *vorticity* anomalies of $1.2\sigma_+$ and $-0.32\sigma_-$, respectively. These figures suggest that the existence of a nominal point of attraction in the convergence-divergence dipole may not be highly fragile to the development of local vorticity anomalies over time. The same inference can be drawn from qualitatively similar

¹⁵One might expect a stronger/weaker vorticity anomaly to develop over time in the convergence/divergence zone, where $|\nabla \cdot \tilde{\mathbf{u}}_b|$ is larger/smaller and much of the entering fluid is hypothetically trapped/untrapped.

streamline plots (not shown) that have been constructed for systems with 2-3 times the positive vorticity anomaly in the convergence zone, and either a proportional or zero change of the negative vorticity anomaly in the divergence zone.

While hardly rigorous or comprehensive, the previous considerations suggest that allowing a dipolar component to exist in the down-tilt convergence field could measurably reduce the critical convergence for core replacement and thus lengthen the time scale for supercritical intensification.

Appendix F: Cloud Resolving CM1 Simulations

F.a Summary of the Data Set

975

976

978

979

980

981

982

984

998

1000

1001

Table F1 summarizes the subset of data from S22 that is used in section 4b as a basis for assessing 985 the adequacy of the diabatic forcing used for this study. The left-most column lists the simulations that are included in the data set. The naming convention is equivalent to that found in S22. The 987 prefix indicates whether the sea-surface temperature is 26 (T26), 28 (T28) or 30 (T30) degrees 988 Celsius. The first two letters of the suffix indicate whether the simulation is low resolution (LR) or high resolution (HR); the former (latter) has a grid spacing equal to (half of) that used herein. The 990 terminal letter (A,B, etc.) is used to distinguish simulations with the same SST and resolution, but 991 different initial conditions.¹⁶ The second column specifies the method used to create the initial tilt, and the magnitude of the initial tilt vector ($|\mathbf{x}_{ml,0}|$). The initialization methods (DSPD and ISPD) are explained in S22. The third column shows the 6-h time periods during which data are 994 collected for Fig. 18; needless to say, time is measured from when the simulation is initialized. The 995 last column gives the maximum azimuthally averaged tangential surface velocity of the tropical cyclone (v_{sm}) , time averaged over the analysis period to the left. 997

F.b Tilt Vector and Heating Parameters

The vortex centers required to compute the tilt vector \mathbf{x}_{ml} and heating displacement ℓ for tropical cyclones in the cloud resolving CM1 simulations are obtained by the procedure explained in SM20,

¹⁶T30-HRD (marked by an asterisk) was conducted for S22, but inadvertently left out of the list of simulations used by the analysis software.

S22 Simulation Name	Initialization Method, Tilt (km)	Analysis Periods (h)	$\langle v_{sm} \rangle_t$ (m s ⁻¹)
T26-HRA	DSPD, 367	226-232	12.8
		283-289	17.6
T26-HRB	DSPD, 182	46-52	17.2
		114-120	17.7
T26-LRB	DSPD, 272	72-78	16.0
T28-HRA	DSPD, 367	37-43	12.1
		160-166	16.8
T28-HRB	DSPD, 282	85-91	16.5
T28-LRA	DSPD, 365	84-90	15.3
T28-LRB	ISPD, 278	48-54	18.2
T30-HRA	DSPD, 367	18-24	12.8
		61-67	17.3
T30-HRD*	DSPD, 282	14-20	14.9
		30-36	20.2
T30-LRA	DSPD, 365	36-42	17.5

TABLE F1. Synopsis of the cloud resolving tropical cyclone simulations analyzed in section 4b. See text for discussion.

which differs in only a few minor details from the procedure used for the diabatically forced tropical 1003 cyclones considered herein. Further elaboration is deemed unnecessary.

1005

1006

1007

1009

1011

The down-tilt heating center of a cloud resolving CM1 simulation is obtained from the following formula:

$$\mathbf{x}_f \equiv \frac{1}{Q_+} \iiint_V dV \max(\rho_d q, 0) \mathbf{x}, \tag{F1}$$

in which $q \equiv TDs_d/Dt$, T (in the present context) is absolute temperature, Ds_d/Dt is the material 1008 derivative of the specific dry entropy s_d , ρ_d is the mass density of dry air, \mathbf{x} is the horizontal position vector, and 1010

$$Q_{+} \equiv \iiint_{V} dV \max \left(\rho_{d} q, 0 \right). \tag{F2}$$

The integration volume V is centered at \mathbf{x}_m , has a radius of 250 km, and extends vertically from 1 to 16 km above sea-level. Although V may extend well into the up-tilt sector of the vortex, 1013 \mathbf{x}_f generally falls well within the cluster of down-tilt convection owing to the relative paucity of 1014 convective latent heat release elsewhere in the tropical cyclone. In section 4b, the values of \mathbf{x}_m

and $\rho_d q$ that are used in the preceding formula for \mathbf{x}_f are either 2-h [Figs. 17 (top row) and 18] or 6-h [Fig. 17 (bottom row)] time averages.

The mean vertically integrated heating density appearing in Fig. 18c is given by

$$Q = \frac{1}{A} \iint_A dA \int_{z_{bot}}^{z_{top}} dz \rho_d q.$$
 (F3)

In the preceding formula, A is the horizontal area within a 100-km radius of \mathbf{x}_f , $z_{bot} = 1$ km, and $z_{top} = 16$ km.

References

1018

1022

- Alland, J.J., B.H. Tang, K.L. Corbosiero, and G.H. Bryan, 2021a: Combined effects of midlevel dry air and vertical wind shear on tropical cyclone development. Part I: Downdraft ventilation. *J. Atmos. Sci.*, **78**, 763-782.
- Alland, J.J., B.H. Tang, K.L. Corbosiero, and G.H. Bryan, 2021b: Combined effects of midlevel dry air and vertical wind shear on tropical cyclone development. Part II: Radial ventilation. *J. Atmos. Sci.*, **78**, 783-796.
- Alvey III, G.R., E. Zipser, and J. Zawislak, 2020: How does Hurricane Edouard (2014) evolve toward symmetry before rapid intensification? A high-resolution ensemble study.

 J. Atmos. Sci., 77, 1329-1351.
- Alvey III, G.R., M. Fischer, P. Reasor, J. Zawislak, and R. Rogers, 2022: Observed processes underlying the favorable vortex repositioning early in the development of Hurricane Dorian (2019). *Mon. Wea. Rev.*, **150**, 193-213.
- Bell, M.M., M.T. Montgomery, and K.A. Emanuel, 2012: Air-sea enthalpy and momentum exchange at major hurricane wind speeds observed during CBLAST. *J. Atmos. Sci.*, **69**, 3197–3222.
- Bryan, G.H., and J.M. Fritsch, 2002: A benchmark simulation for moist nonhydrostatic numerical models. *J. Atmos. Sci.*, **130**, 2917-2928.

- Chen, X., Y. Wang, J. Fang, and M. Xue, 2018: A numerical study on rapid intensification 1041 of Typhoon Vicente (2012) in the South China Sea. Part II: Roles of inner-core processes. 1042 J. Atmos. Sci., 75, 235-255. 1043
- DeMaria, M., 1996: The effect of vertical shear on tropical cyclone intensity change. J. At-1044 mos. Sci., **53**, 2076-2088. 1045
- Dörffel, T., A. Papke, R. Klein, N. Ernst, and P.K. Smolarkiewicz, 2021: Dynamics of tilted 1046 atmospheric vortices under asymmetric diabatic heating. Theor. Comput. Fluid Dyn., 35, 1047 831-873. 1048
- Dunion, J.P., 2011: Rewriting the climatology of the tropical North Atlantic and Caribbean 1049 Sea atmosphere. *J. Climate*, **24**, 893-908. 1050
- Emanuel, K., 2018: 100 years of progress in tropical cyclone research. *Meteor. Monographs*, 1051 **59**, 15.1-68. 1052
- Enagonio, J., and M.T. Montgomery, 2001: Tropical cyclogenesis via convectively forced 1053 Rossby waves in a shallow-water primitive equation model. J. Atmos. Sci., 58, 685-706. 1054
- Finocchio, P.M., S.J. Majumdar, D.S. Nolan, and M. Iskandarani, 2016: Idealized tropical 1055 cyclone responses to the height and depth of environmental vertical wind shear. *Mon. Wea.* 1056 *Rev.*, **144**, 2155-2175. 1057
- Fischer, M.S., R.F. Rogers, P.D. Reasor, J.P. Dunion, 2021: Relationships between vortex tilt, 1058 convective structure, and intensity change in early-stage tropical cyclones. In 34th Conf. on 1059 *Hurricanes and Tropical Meteorology*, AMS.
- Fischer, M.S., P.D. Reasor, R.F. Rogers, and J.F. Gamache, 2022: An analysis of tropical cyclone vortex and convective characteristics in relation to storm intensity using a novel airborne doppler radar database. *Mon. Wea. Rev.*, early release. 1063

1061

Fu, H., Y. Wang, M. Riemer, and Q. Li, 2019: Effect of unidirectional vertical wind shear on 1064 tropical cyclone intensity change—Lower-layer shear versus upper-layer shear. J. Geophys. Res., **124**, 6265–6282. 1066

- Gu, J.F., Z.M. Tan, and X. Qiu, 2019: Intensification variability of tropical cyclones in directional shear flows: Vortex tilt–convection coupling. *J. Atmos. Sci*, **76**, 1827-1844.
- Jones, S.C., 1995: The evolution of vortices in vertical shear. I: Initially barotropic vortices. *Quart. J. Roy. Meteor. Soc.*, **121**, 821-851.
- Kimball, S.K., and M.S. Mulekar, 2004: A 15-year climatology of North Atlantic tropical cyclones. Part I: Size parameters. *J. Climate*, **17**, 3555-3575.
- Kimberlain, T.B., E.S. Blake, and J.P. Cangialosi, 2016: National Hurricane Center tropical cyclone report: Hurricane Patricia. NOAA/NWS Rep. EP202015.
- Molinari, J., D. Vollaro, and K.L. Corbosiero, 2004: Tropical cyclone formation in a sheared environment: A case study. *J. Atmos. Sci*, **61**, 2493-2509.
- Molinari, J., and D. Vollaro, 2010: Rapid intensification of a sheared tropical storm. *Mon.*Wea. Rev., **138**, 3869-3885.
- Möller, J.D., and M.T. Montgomery, 1999: Vortex Rossby waves and hurricane intensification in a barotropic model. *J. Atmos. Sci.*, **56**, 1674-1687.
- Möller, J.D., and M.T. Montgomery, 2000: Tropical cyclone evolution via potential vorticity anomalies in a three-dimensional balance model. *J. Atmos. Sci.*, **57**, 3366-3387.
- Montgomery, M.T., and J. Enagonio, 1998: Tropical cyclogenesis via convectively forced vortex rossby waves in a three-dimensional quasigeostrophic model. *J. Atmos. Sci.*, **55**, 3176-3207.
- Montgomery, M.T., and R.K. Smith, 2014: Paradigms for tropical cyclone intensification. *Aust. Meteor. Ocean. Journ.*, **64**, 37-66.
- Nguyen, L.T., and J. Molinari, 2015: Simulation of the downshear reformation of a tropical cyclone. *J. Atmos. Sci.*, **72**, 4529-4551.
- Nguyen, L.T., R.F. Rogers, and P.D. Reasor, 2017: Thermodynamic and kinematic influences on precipitation symmetry in sheared tropical cyclones: Bertha and Cristobal (2014). *Mon.*Wea. Rev., **145**, 4423-4446.

- Nolan, D.S., Y. Moon and D.P. Stern, 2007: Tropical cyclone intensification from asymmetric convection: Energetics and efficiency. *J. Atmos. Sci.*, **64**, 3377-3405.
- Nolan, D.S., 2011: Evaluating environmental favorableness for tropical cyclone development with the method of point-downscaling. *J. Adv. Model. Earth Syst.*, **3**, M08001:1-28.
- Onderlinde, M.J., and D.S. Nolan, 2016: Tropical cyclone-relative environmental helicity and the pathways to intensification in shear. *J. Atmos. Sci.*, **73**, 869-890.
- Päschke, E., P. Marschalik, P., A.Z. Owinoh, and R. Klein, 2012: Motion and structure of atmospheric mesoscale baroclinic vortices: dry air and weak environmental shear. *J. Fluid Mech.*, **701**, 137-170.
- Pendergrass, A.G., and H.E. Willoughby, 2009: Diabatically induced secondary flows in tropical cyclones. Part I: Quasi-steady forcing. *Mon. Wea. Rev.*, **137**, 805-821.
- Rappin, E.D., and D.S. Nolan, 2012: The effect of vertical shear orientation on tropical cyclogenesis. *Q. J. R. Meteorol. Soc.*, **138**, 1035-1054.
- Reasor, P.D., M.T. Montgomery, and L.D. Grasso, 2004: A new look at the problem of tropical cyclones in shear flow: vortex resiliency. *J. Atmos. Sci.*, **61**, 3-22.
- Reasor, P.D., R. Rogers, and S. Lorsolo, 2013: Environmental flow impacts on tropical cyclone structure diagnosed from airborne Doppler radar composites. *Mon. Wea. Rev.*, 1110 141, 2949-2969.
- Riemer, M., M.T. Montgomery, and M.E. Nicholls, 2010: A new paradigm for intensity modification of tropical cyclones: Thermodynamic impact of vertical wind shear on the inflow layer. *Atmos. Chem. Phys.*, **10**, 3163-3188.
- Rios-Berrios, R., C.A. Davis, and R.D. Torn and 2018: A hypothesis for the intensification of tropical cyclones under moderate vertical wind shear. *J. Atmos. Sci.*, **75**, 4149-4173.
- Rogers, R.F., P.D. Reasor, J.A. Zawislak, and L.T. Nguyen, 2020: Precipitation processes and vortex alignment during the intensification of a weak tropical cyclone in moderate vertical shear. *Mon. Wea. Rev.*, **148**, 1899-1929.
- Schecter, D.A., 2020: Distinct intensification pathways for a shallow-water vortex subjected to asymmetric "diabatic" forcing. *Dyn. Atmos. Oceans*, **91**, 101156:1-25.

- Schecter, D.A., and K. Menelaou, 2020: Development of a misaligned tropical cyclone. *J. Atmos. Sci.*, **77**, 79-111.
- Schecter, D.A., 2022. Intensification of tilted tropical cyclones over relatively cool and warm oceans in idealized numerical simulations. *J. Atmos. Sci.*, **79**, 485-512.
- Schubert, W.H., and J.J. Hack, 1982: Inertial stability and tropical cyclone development. *J. Atmos. Sci.*, **39**, 1687-1697.
- Shapiro, L.J., and H.E. Willoughby 1982: The response of balanced hurricanes to local sources of heat and momentum. *J. Atmos. Sci.*, **39**, 378-394.
- Smith, R.K., M.T. Montgomery, and H. Zhua, 2005: Buoyancy in tropical cyclones and other rapidly rotating atmospheric vortices. *Dyn. Atmos. and Oceans*, **40**, 189-208.
- Stevenson, S.N., K.L. Corbosiero, and J. Molinari, 2014: The convective evolution and rapid intensification of Hurricane Earl (2010). *Mon. Wea. Rev.*, **142**, 4364-4380.
- Tao, D., and F. Zhang, 2014: Effect of environmental shear, sea-surface temperature, and ambient moisture on the formation and predictability of tropical cyclones: An ensemble-mean perspective. *J. Adv. Model. Earth Syst.*, **6**, 384-404.
- Vigh, J.L., and W.H. Schubert, 2009: Rapid development of the tropical cyclone warm core. *J. Atmos. Sci.*, **66**, 3335-3350.
- Wang, Y., Y. Li, and J. Xu, 2021. A new time-dependent theory of tropical cyclone intensification. *J. Atmos. Sci.*, **78**, 3855-3865.
- Zawislak, J., H. Jiang, G.R. Alvey, E.J. Zipser, R.F. Rogers, J.A. Zhang, and S.N. Stevenson,
 2016: Observations of the structure and evolution of Hurricane Edouard (2014) during intensity change. Part I: Relationship between the thermodynamic structure and precipitation.

 Mon. Wea. Rev., 144, 3333-3354.